MASTER'S THESIS

LUND UNIVERSITY

LUND TEKNISKA HÖGSKOLA

DEPARTMENT OF PHYSICS

Few-cycle Pulse Generation using Bulk Multi-pass Cells

Author:
Sara Rushe Palacios

Supervisor:
Anne-Lise Viotti

Co-supervisors:
Saga Westerberg
Gaspard Beaufort

Examiner:
Lars Rippe

LARP:
623 (2026)

Division of Atomic Physics
Lund Institute of Physics, Lund University
Lund, Sweden
May 2026

Abstract

Few-cycle laser pulses are fundamental for tracking ultrashort motions such as electron dynamics and achieving stronger fields. They are also extensively used to perform high-harmonic generation and in attosecond science. However, generating stable and high quality few-cycle pulses requires a simultaneous control of bandwidth and dispersion. The generation of few-cycle pulses in an efficient manner is also quite challenging. This thesis looks into the generation of few-cycle pulses through a cascaded multi-pass cell post-compression scheme.

The system consists of a two-stage multi-pass cell setup with bulk fused silica as the nonlinear medium. The tasks for this project were focused on the second stage where special attention was set on the dispersion management using chirped mirrors within the cavity and compression stage as well as further material placement for higher-orders of dispersion compensation.

Using the entire setup, a total compression from 220 fs to 6.2 fs was achieved rendering a total compression factor of 34.5 providing a few-cycle laser pulse with good spatial quality.

The results from this project aim towards proving the worth of cascaded bulk multi-pass cells systems for pulse compression, providing a stable, robust and energy-scalable setup for the generation of few-cycle laser pulses that can be further used for high-harmonic generation.

Popular Science Abstract

Lasers are research tools which are becoming progressively more important every year, with many applications in fields such as: surgery, electronics, ophthalmology, telecommunications, defense, research, etc. All lasers are based on the same principle, which is light amplification by stimulated emission. In other words, light triggering the emission of more light. The output, on the other hand, can vary depending on the use. For instance, the color of the beam that emerges can be different, the power can be higher or lower or the beam can be continuous or pulsed.

For this project, the starting point was a pulsed laser, which emits tiny bursts of energy of a certain color. By "tiny" we actually mean extremely short time durations, specifically in the femtosecond scale. One femtosecond is an incredibly small number, which, in perspective has the same relation to a single second as one second has to 32 million years. This femtosecond time scale in physics is referred to as ultrafast, or similarly ultrashort.

For many of the applications mentioned before as well as for research purposes the duration of the light pulses needs to be ultrashort, the frequency at which those pulses are emitted needs to be high and the pulses need to carry enough power. For that, industrial-grade laser systems are preferred because they offer much higher average powers and better efficiencies. But the drawback is that their laser pulses have slightly longer time durations (hundreds of femtoseconds), when we actually want below 10 femtoseconds. So, how can these bursts be shortened even further?

The key is to consider the colors which are traveling in the burst. Although we previously mentioned that there was a single color in the burst, we can extend this to include many shades of the same color being emitted from the laser. This is akin to having a long pulse in time, as a pulse with a narrow range of colors tends to last longer, while a shorter pulse encompasses a broader range of colors.

To shorten this pulse in time, we need to pack many more colors, and their various shades, into a single laser burst. This can be visualized as a race: initially, there is only one runner, but as the race progresses, more runners join in and run together.

Returning to the concept of the laser pulse, the way to create these new colors involves using specific materials that undergo changes in their properties when subjected to extremely high intensities. This process leads to the generation of new colors. Consequently, the initial pulse with one color entering the material (like one runner beginning the race) will exit with many colors traveling together (like multiple runners finishing the race).

However, not all runners (nor colors) run at the same speed: different colors travel at different velocities. To achieve a compressed laser pulse in time, we need all the colors to arrive simultaneously. This requires us to hold some colors back to adjust the relative delays. This entire procedure is performed by manipulating various optical elements, taking into account their properties and how they will interact with light, which is precisely what the optical setup designed in this thesis aims to accomplish.

This master's thesis aims to compress the duration of a laser pulse of 50 femtoseconds to under 10 femtoseconds by means of a technique that compresses pulses in time. Specifically, a multi-pass cell is built. This refers to a mirror chamber that makes light travel back and forth many times, with the material to carry out the color-adding in the chamber. A long pulse in time will be made significantly shorter to have an extremely ultrashort laser pulse useful for applications such as capturing images of chemical reactions or probing ultrafast electron dynamics.

Acknowledgements

I would like to start by expressing my sincere gratitude to my supervisors: Anne-Lise, Saga and Gaspard. Anne-Lise, thank you very much for proposing such an interesting project and for your guidance during the entire time working together. I am especially grateful for all the discussions and clear explanations, as well as for all your advice and time. I have learnt a great deal from this experience and, for that I will be forever grateful. Thank you Saga, for being an incredible co-supervisor, for sharing your MPC knowledge, for being so patient with me in the lab and for answering my countless questions. I am so thankful for all your advice and insights (not only in physics but also life in general) and I have enjoyed working by your side so incredibly much! And thank you for always saving me when I thought I had completely misaligned the MPC... Thank you also to Gaspard for being a fantastic co-supervisor. I am very grateful for your guidance and for always answering my questions with so much patience as well. Thank you for always having a smile to give in the mornings. I will never forget my first ever experience with the OSA with you guys! I would also like to thank Melvin, for your constant help and for replying the never ending questions I was always asking. You never failed to solve my coding-related questions, which were many! Working in the D-Lab has been genuinely an enjoyable experience thanks to all of you! I would also like to thank all the members of the *Laser Meetings* and *D-Lab Meetings* for all the meaningful discussions and valuable feedback throughout the year. And thanks also to all the people in the Atomic Division for the welcoming and warm environment. All the laughs, chats and shared lunches made this experience all the more enjoyable.

I would also like to thank the people outside of the Physics Department who have also supported me during this year and project. Thanks to all my friends in my promotion of the Master's in Photonics - I am so happy that this experience brought us together and it was truly so much fun sharing classes as a group.

And last but certainly not least, thank you to my family. Thank you for your constant support and guidance. And thank you for all your love, always.

Contents

1 Introduction **1**
1.1 Motivation . . . 2
1.2 Objective . . . 3

2 Theoretical Background **4**
2.1 Gaussian Beam Optics . . . 4
2.1.1 Resonators . . . 5
2.2 Ultrafast Optics . . . 7
2.2.1 Dispersion and Pulse Propagation . . . 8
2.2.2 Few-cycle Regime . . . 9
2.3 Non-linear Optics . . . 10
2.3.1 Optical Kerr Effect . . . 10
2.4 Post-compression Techniques . . . 12
2.5 Ultrashort Pulse Characterization . . . 14
2.5.1 Temporal Pulse Characterization . . . 14
2.5.2 Spatial Characterization . . . 15

3 Multi-pass cell (MPC) **17**
3.1 The Herriott Configuration . . . 17
3.2 Beam Sizes . . . 18
3.3 Nonlinear Medium: Gas or Bulk . . . 19
3.4 MPC for Few-cycle . . . 20
3.5 Cavity Dispersion Design . . . 21
3.5.1 Analysis of Nonlinear Propagation Simulations . . . 23

4 Experimental Setup & Results **26**
4.1 The Laser Source . . . 26
4.2 MPC 1 . . . 26
4.3 MPC 2 . . . 30
4.3.1 Spectral Broadening Results . . . 30
4.3.2 Pulse Compression Results . . . 32
4.3.3 Laser Beam Profile . . . 39

5 Conclusions and Outlook **42**
5.1 Conclusions . . . 42
5.2 Outlook . . . 43

Bibliography **47**

Nomenclature

Abbreviations

BBO	Beta-Barium Borate
CEP	Carrier Envelope Phase
CM	Chirped Mirrors
CPA	Chirped Pulse Amplification
D-Scan	Dispersion-scan
FM	Frequency Modulated
FROG	Frequency Resolved Optical Gating
FS	Fused Silica
FTL	Fourier Transform Limit
FWHM	Full Width at Half Maximum
GD	Group Delay
GDD	Group Delay Dispersion
HCF	Hollow-core Fibers
HHG	High-order Harmonic Generation
KDP	Potassium Dihydrogen Phosphate
LASER	Light Amplification by Stimulated Emission of Radiation
LIDT	Laser-Induced Damage Threshold
MPC	Multi-pass Cell
OPCPA	Optical Parametric Chirped Pulse Amplification
OSA	Optical Spectrum Analyzer
ROC	Radius of Curvature
SF	Self-Focusing
SHG	Second Harmonic Generation
SPM	Self-phase Modulation
TFP	Thin-Film Polarizer
THG	Third Harmonic Generation
Ti:Sa	Tittanium Sapphire
TOD	Third Order Dispersion
WP	Waveplate
XUV	Extreme Ultra-Violet
Yb	Ytterbium

List of Figures

1.1 Bulk Multi-pass Cell Sketch consisting of two concave mirrors placed in front of each other forming the cavity where two bulk plates are placed inside symmetrically from the center. 2

2.1 Gaussian beam profile representing the propagation direction z as a function of the radial distance r. Additionally, the color scale represents the normalized strength of the amplitude of the Gaussian function given in Equation 2.1, showing the peak intensity at the beam center. 4
2.2 Laser Resonator Sketch 5
2.3 Resonator Stability Diagram. The graph shows the possible regimes of solutions from Equation 2.11 in green, where resonators are considered stable. The solid red line shows the solutions of this equation for the equality. Some examples of resonators are sketched depending on their stability position. Their location conditions the sign of the radii of curvature of each mirror. 6
2.4 Temporal and spectral representation of laser pulse 7
2.5 Linearly up-chirped (a) and linearly down-chirped (b) optical pulses 8
2.6 Second Harmonic Generation (SHG) 10
2.7 Self-phase modulation (top) and Self-focusing (bottom). For the top image, an incoming pulse with a narrow spectrum is broadened into a wide spectrum while adding a phase shift from the propagation. For the bottom image, the wavefront of a laser beam is represented as the red lines. The incoming beam has a planar wavefront and after the propagation through the Kerr medium acting as a thin lens, the wavefront is curved. 11
2.8 Post-compression Principle. An initial narrow spectrum is broadened through an MPC leading to a broader spectrum with quadratic chirp, which is flattened through a pair of chirped mirrors (CM). 13
2.9 Typical D-Scan Implementation 15

3.1 Herriott Pattern on one Cavity Mirror for N = 15 with Advance Angle for k = N-2 17
3.2 Variation of Beam Size in a Mode-matched Bulk MPC for different pulse energies . 18
3.3 MPC Architecture Schematic for Beam Size Simulation 19
3.4 Schematic of Cascaded MPC System 21
3.5 GDD of CM 1 and 2 as a function of the wavelength. The average GDD is shown in orange and compared to the opposite GDD of a 3 mm thick piece of Fused Silica (dashed red line) calculated from the Sellmeier equations. The cavity mirror data is extracted from the group delay obtained from the mirror manufacturer. 21
3.6 Simulated comparison between Dispersion-compensated Pulse and Non-dispersion-compensated Pulse. For the dispersion compensated scenario, paired CM compensating for the equivalent GDD to 3 mm were taken into account. For the non-dispersion compensated case, non-chirped mirrors were taken into account. 22
3.7 Cell Length as a function of Number of Roundtrips (for a maximum of N = 7 and R = 200 mm) 23
3.8 MPC 2 Output vs Input for an incoming pulse of 50 fs duration and 70 μJ energy. The output pulse duration is 8.4 fs. 24
3.9 Simulation of Spectral Broadening in MPC 2 as a function of the Propagation Length (in Roundtrips). The side color bar represents the normalized spectral evolution . 24
3.10 Simulation of Pulse Energy after Different Roundtrips 25

4.1 Laser Spectrum 26
4.2 MPC 1 Experimental Setup. A1: Attenuation Stage. MMT1: Mode-matching Telescope. M1 and M2: MPC Cavity Mirrors. M3: Collimating Curved Mirror. CM: Chirped Mirrors (Compression Stage) 27
4.3 MPC 1 Result for Incoming Pulse with duration 220 fs and energy E = 100 μJ. The Output Pulse Duration is 50 fs. 28
4.4 MPC 2 Experimental Setup. A2: Attenuation Stage. MMT2: Mode-matching Telescope. M1 and M2: Dispersion Compensating Cavity Mirrors. DS: Delay Stage. CM: Chirped Mirror Compression Stage 29
4.5 Spectral Measurements of MPC 2 at E_{in} = 25 μJ for different FS separation . . . 31
4.6 Spectral Broadening from SPM at different energies and FS plate separation . . . 32
4.7 D-Scan Retrieval E_{in} = 20 μJ FS Plates Separation 10 cm. (a) Measured laser beam map obtained by measuring the spectrum at each insertion of the dispersion elements into the beam path. (b) Retrieved laser beam map acquired after applying the software algorithm. (c) Spectrum of the laser beam for 0 mm insertion, representing no added dispersion. (d) Pulse retrieval corresponding to 0 mm of dispersion added. (e) Spectrum of the laser beam after virtual propagation through -10.8 mm of Fused Silica. (f) Pulse retrieval corresponding to spectrum after virtual propagation through -10.8 mm of Fused Silica compared to Transform Limited Pulse. 34
4.8 D-Scan Retrieval E_{in} = 25 μJ FS Plates Separation 10 cm. (a) Measured laser beam map obtained by measuring the spectrum at each insertion of the dispersion elements into the beam path. (b) Retrieved laser beam map acquired after applying the software algorithm. (c) Spectrum of the laser beam for 0 mm insertion, representing no added dispersion. (d) Pulse retrieval corresponding to 0 mm of dispersion added. (e) Spectrum of the laser beam after virtual propagation through -8.9 mm of Fused Silica. (f) Pulse retrieval corresponding to spectrum after virtual propagation through -8.9 mm of Fused Silica compared to Transform Limited Pulse. 35
4.9 Pulse Shapes for various incoming pulse energies for FS plate separation of 17 cm. The graph was built by overlapping the pulse retrievals acquired at 0 mm insertion of dispersion elements (no dispersion) for different input pulse energies. The color scale represents the intensity normalized by the maximum intensity value of each pulse retrieval. 36
4.10 Pulse Shapes for certain incoming pulse energies for FS plate separation of 17 cm. The pulse retrievals were taken for 0 mm of dispersion insertion in the dispersion-scan. 36
4.12 Pulse Shapes for various incoming pulse energies considering virtual propagation through 5 mm of KDP and 5 mm of FS. The graphs were obtained by overlapping the pulse retrievals acquired at 0 mm dispersion insertion for different input pulse energies. The color scale represents the intensity normalized by the maximum intensity value of each pulse retrieval. 37
4.11 GDD and TOD as a function of wavelength for KDP obtained from the ordinary refractive index (n_o) expression from the Sellmeier equations. A thickness of 2.5 mm of KDP was considered, which will later be implemented experimentally. 37
4.13 Retrieved Output Pulse Temporal Profiles of MPC 2 for certain incoming pulse energies considering virtual propagation through 5 mm of KDP and 5 mm of FS. The pulse retrievals were obtained for 0 mm insertion of dispersion. 38
4.14 D-Scan Retrieval for E_{in} = 68.75 μJ, FS Plates Separation 17 cm, Propagation through 2.5 mm KDP and 1.5 mm FS. The spectrum acquired on the lower left graph is for 0 mm of dispersion insertion. 38
4.15 Collimated Beam Profile of MPC 2 FS for Plate Separation 17 cm 40
4.16 M^2 Measurement of Outcoming Pulse 41
4.17 Measured Focus from MPC 2 Output using a Focusing Lens 41

Chapter 1

Introduction

Over 60 years ago, the first LASER was born [1], an acronym making reference to **L**ight **A**mplification by **S**timulated **E**mission of **R**adiation. As the years have passed scientists have only wanted to push their properties to their limits and observe the outcome. The most common applications in daily life include transmission and processing of information as well as delivering energy. Lasers are still in constant development to improve their characteristics: power, beam quality, wavelength tunability, gain media and output type. The different types of lasers rise from the latter two features. In terms of gain media, there are gas lasers (Helium-Neon Lasers), solid-state lasers (Nd:YAG Lasers, Titanium Sapphire (Ti:Sa) Laser, Ytterbium (Yb) Laser), dye lasers, etc. And, regarding the output it is possible to distinguish between continuous or pulsed. The presence of pulsed lasers has allowed for bursts of energy ranging in duration from milliseconds (1 ms = 10^{-3}s) to attoseconds (1 as = 10^{-18} s). This wide range has led to different sub-intervals, such as ultrashort defined by pulses with up to a few hundreds of femtoseconds (1 fs = 10^{-15} s). Ultrashort laser pulses with high-peak powers have a broad range of applications: laser-based nuclear fusion [2], high harmonic generation (HHG) [3], attosecond science [4], and laser-plasma acceleration [5]. At the end of the 20th century, the most common laser system in the ultrafast regime was the Ti:Sa Laser, known for its large gain bandwidth, pulse durations with values from 10 fs to 100 fs for commercial systems and sub-10 fs for research-oriented systems and energies up to the Joule (J) scale for up to a few Hertz (Hz) of repetition rate. These characteristics had only been achieved after the introduction of *Chirped Pulse Amplification* [6]. However these lasers have recently been replaced by newer systems such as Ytterbium-doped systems. These laser systems are more industrially used while Ti:Sa lasers have always been devoted to research. Ytterbium-based lasers have the advantages of scaling to very high average powers with high efficiency and in a compact manner. Some drawbacks however are the longer pulse durations and limited wavelength tunability. The laser pulses in Ytterbium-based laser systems take values of a few hundred femtoseconds (fs) up to a few picoseconds (ps), a regime called ultrafast.

One solution to achieve shorter pulses and higher peak power is pulse compression, where different techniques have reduced the duration of laser pulses reaching the few-cycle regime. This regime is characterized by the envelope of the laser pulse only accounting for a small number of optical cycles, i.e. the oscillation of the electric field. Although this value depends on the wavelength used ($T = \lambda/c$), the generalization is for the pulses to be below 10 fs. These short pulses are of great interest for a variety of applications, especially for HHG because of their possibility to generate isolated attosecond pulses and to extend the cutoff energy, by increasing the intensity through a compressed pulse [7]. In the past years, there has been a wide development in post-compression techniques. Most are based on self-phase modulation (SPM) as the nonlinear process to achieve the spectral broadening [8]. Some examples are gas-filled hollow-core fibers (HCF) [9], white-light filaments [10], cascaded focus and compression (CASCADE) [11] and Herriott-type multi-pass cell (MPC) [12].

Figure 1.1 shows an example of the geometry of a bulk MPC, which is the type developed in this project. There are different configurations of MPC, altering the geometry, mirror location and even the nonlinear medium of propagation. The case for this project is bulk plates as the nonlinear material. The main principle of MPCs is based on a resonator in which a laser pulse propagates a certain number of passes. This resonator contains a Kerr medium which will introduce a nonlinear

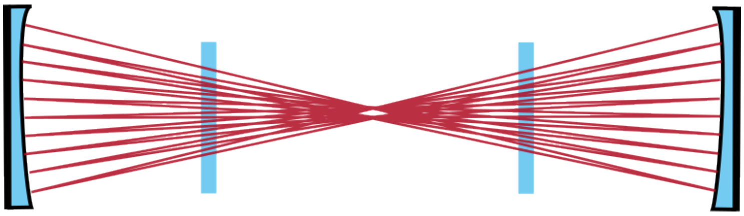

Figure 1.1: Bulk Multi-pass Cell Sketch consisting of two concave mirrors placed in front of each other forming the cavity where two bulk plates are placed inside symmetrically from the center.

phase every time the beam passes through it. The Kerr medium can be solid or gaseous. Bulk MPCs are exploited for lower pulse energies, in the range from 10 μJ to 100 μJ. Meanwhile, gas MPCs are used for higher pulse energies exceeding 100 mJ [13]. Regarding pulse durations, they have successfully compressed pulses down to the femtosecond range from input picosecond durations. Further compression to few femtoseconds are being studied, a regime called *few-cycle*. MPCs have proven worthy for pulse post-compress due to their robust and compact architecture. They allow for a broad range of parameters applicable to laser pulses with a wide energy range (μJ to mJ).

1.1 Motivation

HHG is a process that requires pulses with high intensities to the order of 10^{14} W/cm^2. For many years, the laser of choice for HHG was the Ti:Sa laser, due to its characteristic ultrashort few-cycle pulses. Nevertheless, its repetition rates do not match to those of Yb-based lasers. High-order harmonic generation is a nonlinear optical process that takes place from the interaction of an atom in a gas with a strong laser field. This field will lower the potential energy barrier of the atom allowing electrons from the outer shells of the atom to escape. These electrons will then propagate in a continuum, where they are accelerated by the laser field and after some time can recombine with the ionized atom. All these steps are called *The Three Step Model*: Tunnel Ionization, Acceleration and Recombination [14]. After the process is completed coherent Extreme Ultra-Violet (XUV) radiation is emitted in the form of a train of attosecond pulses. XUV radiation is emitted periodically at each half-cycle, so it results in interferences in the spectral domain (harmonics). If there is only one cycle, it is possible to generate an isolated attosecond pulse.

HHG has a strong dependence on the pulse duration. For instance, the use of single-cycle laser pulses can lead to the generation of isolated attosecond pulses. Additionally, recent studies have shown that the conversion efficiency of HHG is also scaled with pulse duration. According to Westerberg et al. (2025) [15], the highest harmonic generation conversion efficiency (ε_{HHG}) is achieved when the laser intensity reaches the phase matching critical intensity. As a consequence, the conversion efficiency depends on the laser pulse duration as follows:

$$\varepsilon_{\text{HHG}} = \frac{1}{\sqrt{\tau_{\text{opt}}}} \tag{1.1}$$

where τ_{opt} represents the optimal laser pulse duration achieved at the critical intensity for phase matching in the cases of a short gas target and high pressure regime. Studying Equation 1.1 it is possible to state that short pulses will provide the maximum conversion efficiencies provided they also reach the phase matching intensity. In study [15], a tunable femtosecond laser system was achieved with pulse durations from 40 fs to 180 fs. This large range was achieved with an Yb-doped laser followed by an MPC for tunable compressed pulse duration.

This study was not performed for shorter pulse durations, which would in theory lead to even higher conversion efficiencies. Thus there is a need to push the limit of pulse post-compression towards the generation of few-cycle laser pulses. Cascading MPCs has shown very promising results in achieving few-cycle laser pulses. Currently the shortest output laser pulse achieved through a two-stage cascade of gas-filled MPCs has been achieved by Müller et al. (2021) [16], rendering a compressed pulse with duration 6.9 fs, providing a total compression factor of 29. Solid-state-based MPCs have also proven worthy especially due to their capability for robust and efficient generation of intense few-cycle pulses at modest energies. For instance Viotti et al. (2023) [17]

showed a two-stage system of all-bulk multi-pass cells cascaded rendering a compression factor of 120, leading to outcoming pulses with 8.2 fs duration.

The goal of this master's thesis project is to build a cascaded setup of all-bulk MPCs to achieve an output pulse in the few-cycle regime. This pulse will have as future application the generation of higher-order harmonics. Solid-state MPCs are chosen over gas-filled due to their higher nonlinearities, ensuring large spectral broadening as well as a robust and compact setup. An added advantage of bulk MPCs is the lack of need to build a vacuum chamber and install gas lines.

1.2 Objective

The experimental setup, consists of two bulk MPC stages for pulse post-compression of 220 fs towards sub-10 fs. My project was dedicated to the design, simulation, alignment and characterization of the second stage, which aimed at delivering the few-cycle laser pulses. I specifically studied the output pulse characteristics as a function of input pulse energy and the location of the nonlinear media in the cell.

Chapter 2

Theoretical Background

In this second chapter a theoretical overview of the physics implemented for this thesis is given. The main concepts include Gaussian beam optics, Ultrashort laser pulses and their characteristics followed by a brief introduction into Nonlinear Optics focusing on the processes included in this thesis. The very final mention in this chapter deals with different techniques for pulse post-compression followed by methods for ultrashort pulse characterization.

2.1 Gaussian Beam Optics

The electic field of a laser beam can be approximated by a Gaussian function where the amplitude is given by the expression

$$\mathcal{A}(r,z) = \mathcal{A}_0 \frac{\mathrm{w}_0}{\mathrm{w}(z)} e^{\frac{-r^2}{\mathrm{w}^2(z)}} e^{-ikz+ik\frac{r^2}{2R(z)}-i\phi(z)} \tag{2.1}$$

where $r^2 = x^2+y^2$ and k represents the wavenumber. We can define the beam size $\mathrm{w}(z)$ at different positions z as

$$\mathrm{w}(z) = \mathrm{w}_0\sqrt{1+\left(\frac{z}{z_R}\right)^2} \tag{2.2}$$

here w_0 is the beam waist radius and $z_R = \frac{\pi \mathrm{w}_0^2}{\lambda}$ is the Rayleigh length, representing the distance between the position of the focus point and the location at which the beam cross-section doubles its size, as shown in Figure 2.1.

Similarly to the expression of the beam size, we can express the radius of curvature at different locations as

$$R(z) = z\left(1+\left(\frac{z}{z_R}\right)^2\right) \tag{2.3}$$

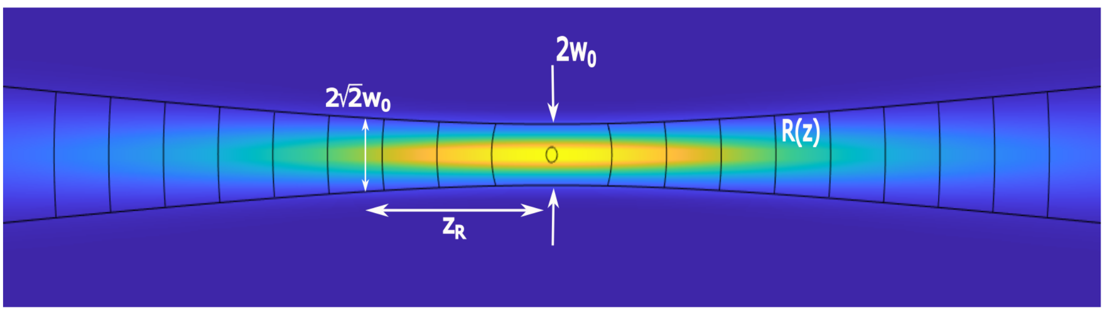

Figure 2.1: Gaussian beam profile representing the propagation direction z as a function of the radial distance r. Additionally, the color scale represents the normalized strength of the amplitude of the Gaussian function given in Equation 2.1, showing the peak intensity at the beam center.

Free space propagation for a distance d	$\begin{bmatrix} 1 & d \\ 0 & 1 \end{bmatrix}$
Reflection from a curved mirror (radius R)	$\begin{bmatrix} 1 & 0 \\ -2/R & 1 \end{bmatrix}$
Transmission through a thin lens (focal length f)	$\begin{bmatrix} 1 & 0 \\ -1/f & 1 \end{bmatrix}$

Table 2.1: ABCD matrices for basic optical elements

In Equation 2.1 we can also observe in the final exponential a component representing the phase, $\phi(z)$. This represents the Gouy phase shift which is also related to the Rayleigh length by $\phi(z) = \arctan\left(\frac{z}{z_R}\right)$.

An analogous version of writing the complex envelope of a Gaussian Beam, other than Equation 2.1 is

$$\mathcal{A}(r) = \frac{\mathcal{A}_0}{q(z)} e^{-ik\frac{r^2}{2q(z)}} \tag{2.4}$$

From this expression we notice the appearance of a term $q(z)$ defined as the q-parameter, a useful tool in order to relate the real and imaginary components of the complex envelope:

$$\frac{1}{q(z)} = \frac{1}{R(z)} - i\frac{\lambda}{\pi\omega(z)^2} \tag{2.5}$$

$$q(z) = z + \frac{i\pi\omega_0^2}{\lambda} = z + iz_R. \tag{2.6}$$

where λ defines the wavelength of the light beam.

To describe how this q-parameter changes as the laser beam passes through an optical setup made up of different elements it is necessary to introduce the ray-transfer matrices of ray optics:

$$\begin{bmatrix} x_2 \\ \theta_2 \end{bmatrix} = \begin{bmatrix} A & B \\ C & D \end{bmatrix} \begin{bmatrix} x_1 \\ \theta_1 \end{bmatrix} \tag{2.7}$$

with x_2 and θ_2 being the out-coming beam position and angle, respectively. Similarly, x_1 and θ_1 represent the incoming beam position and angle, respectively. The q-parameter can be expressed as well in terms of the $ABCD$ matrix as

$$q_2 = \frac{Aq_1 + B}{Cq_1 + D} \tag{2.8}$$

Some examples of $ABCD$ matrices and the ones used for this Thesis can be seen in Table 2.1. With these matrices it is also possible to represent more complex systems by multiplying them, as will be shown in the following chapter.

2.1.1 Resonators

An MPC, due to its setup, resembles a spherical mirror resonator and thus can be approximated by the same properties. Specifically, an MPC can be compared to a resonator made up of two concave mirrors with radii of curvature R1 and R2 (Figure 2.2). This setup makes up a periodic optical setup where the period would be a roundtrip of two reflections off of the mirrors and a propagation of distance L. Because of this, it is possible to use the matrix representation as specified previously. Specifically, the matrix of one full roundtrip is obtained by

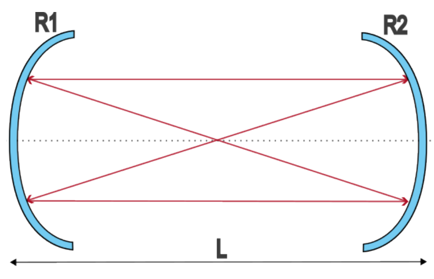

Figure 2.2: Laser Resonator Sketch

the multiplication of the matrix from the reflection of the left mirror, a propagation for a distance L (length between the resonator mirrors), the reflection from the right mirror and finally the back propagation the same length L.

$$\begin{bmatrix} A & B \\ C & D \end{bmatrix} = \begin{bmatrix} 1 & L \\ 0 & 1 \end{bmatrix} \begin{bmatrix} 1 & 0 \\ 2/R_2 & 0 \end{bmatrix} \begin{bmatrix} 1 & L \\ 0 & 1 \end{bmatrix} \begin{bmatrix} 1 & 0 \\ 2/R_1 & 0 \end{bmatrix} \tag{2.9}$$

Writing this matrix in the form of Equation 2.8

$$q_{out} = \frac{Aq_{in} + B}{Cq_{in} + D} = q_{in} \tag{2.10}$$

The final equality relating q_{out} back to q_{in} is called the self-replication criterion and helps describe the beam at any point inside the resonator since q_{in} is the eigenmode. This property of resonator optics is also present in the MPC used for spectral broadening, as is the case of this thesis.

In order for a resonator to be stable, and therefore similarly an MPC, a stability condition must be satisfied, as shown in Figure 2.3. This constraint is dependent on the length of the resonator L and the radius of curvature of both mirrors, R_1 and R_2.

$$0 \leq \left(1 - \frac{L}{R_1}\right)\left(1 - \frac{L}{R_2}\right) \leq 1 \tag{2.11}$$

Additionally, for a symmetric resonator where both radii of curvature of the mirrors are the same, the stability condition can be rewritten as $0 \leq L \leq 2R$. This specific case of both mirrors having the same radius of curvature is taking place in this project.

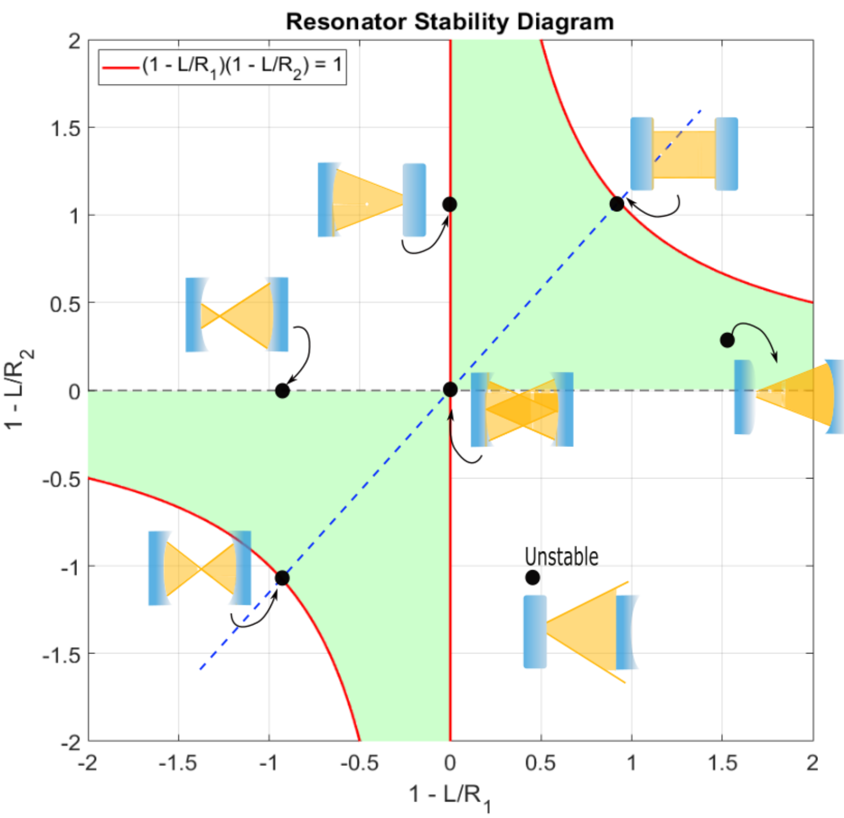

Figure 2.3: Resonator Stability Diagram. The graph shows the possible regimes of solutions from Equation 2.11 in green, where resonators are considered stable. The solid red line shows the solutions of this equation for the equality. Some examples of resonators are sketched depending on their stability position. Their location conditions the sign of the radii of curvature of each mirror.

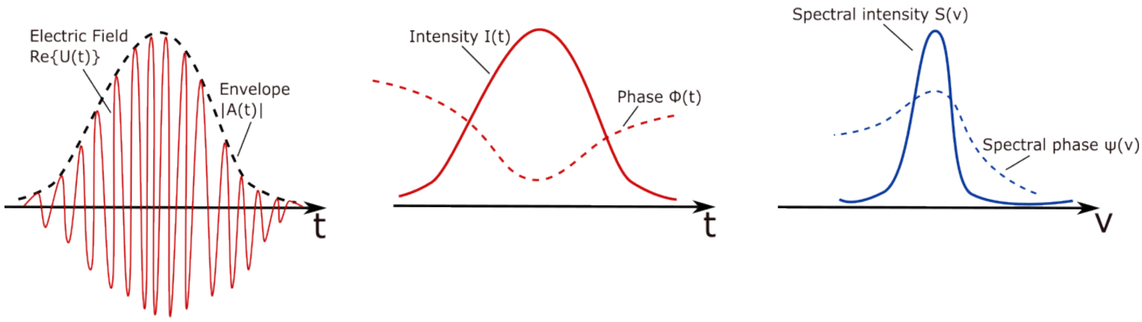

Figure 2.4: Temporal and spectral representation of laser pulse

Left: Temporal envelope and Electric Field. Center: Time dependent Intensity and Temporal Phase. Right: Spectral Intensity and Spectral Phase of a Laser Pulse

2.2 Ultrafast Optics

In the field of optics, the term *ultrashort* is normally reserved for pulses with a time duration in the range of a few picoseconds (1 ps = 10^{-12} s) to attoseconds. The study of ultrafast optics focuses on the properties of these ultrashort laser pulses. Most femtosecond pulses are achieved through mode-locked lasers [18]. Unlike continuous wave lasers, pulsed lasers have an optical intensity that depends on time.

A light pulse can be described by an electric field with finite time duration. It can also be represented by the complex wavefunction (Figure 2.4 (left))

$$\mathcal{U}(t) = \mathcal{A}(t)e^{i\omega_0 t} \tag{2.12}$$

with ω_0 being the central angular frequency related to the central frequency ν_0 as $\omega_0 = 2\pi\nu_0$. $\mathcal{A}(t)$ is the complex envelope of the optical pulse and gives rise to several other parameters, such as the phase $\phi(t) = \arg(\mathcal{A}(\mathrm{t}))$ and the intensity of the pulse $I(t) = |\mathcal{A}(t)|^2$ (Figure 2.4 (center)). The temporal width of the pulse is given as τ_{FWHM} and is defined as the full-width at half-maximum (FWHM) of the temporal intensity profile. Converting the optical pulse into the spectral domain by taking the Fourier Transform, we have

$$\mathcal{V}(\nu) = \int \mathcal{U}(t)e^{-i2\pi\nu t}dt = |\mathcal{V}(\nu)|e^{-i\psi(v)} \tag{2.13}$$

where we can define the spectral intensity as

$$\mathcal{S}(\nu) = |\mathcal{V}(\nu)|^2 \tag{2.14}$$

and $\psi(\nu)$ as the spectral phase (Figure 2.4 (right)). Similarly, in the spectral domain the spectral width is defined as $\Delta\nu$ and is also the FWHM of the spectral intensity spectrum.

As a final characteristic of the optical pulse we have the instantaneous angular frequency [19], which is the time derivative of the phase of $\mathcal{U}$(t):

$$\omega_i = \omega_0 + \frac{d\phi}{dt} \tag{2.15}$$

If the instantaneous angular frequency is time varying, then we can say that an optical pulse is frequency modulated (FM) or chirped. If it is an increasing function of time then the pulse is up-chirped (Figure 2.5 (a)) and for the opposite, we have a down-chirped pulse (Figure 2.5 (b)). It is possible to define a chirp parameter to measure this more clearly:

$$a = \frac{1}{2}\frac{d^2\phi}{dt^2}\tau^2 \tag{2.16}$$

where τ is a real parameter. Similarly if a>0 the pulse is up-chirped and when a<0 it is down-chirped.

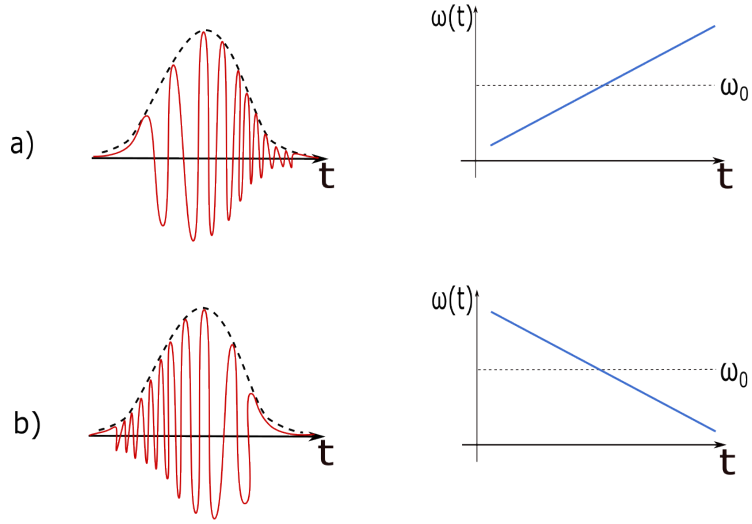

Figure 2.5: Linearly up-chirped (a) and linearly down-chirped (b) optical pulses

An unchirped or transform-limited Gaussian pulse can be written as Equation 2.17.

$$\mathcal{A}(t) = \mathcal{A}_0 e^{-\frac{t^2}{\tau^2}} \tag{2.17}$$

From this primary equation we can find all the parameters characteristic for the temporal and spectral descriptions. The intensity can be written as

$$I(t) = I_0 e^{\left(-\frac{2t^2}{\tau^2}\right)} \tag{2.18}$$

The temporal width is thus $\tau_{\mathrm{FWHM}} = \tau\sqrt{2\ln 2}$ and the spectral width is $\Delta\nu = 0.375/\tau = 0.44/\tau_{\mathrm{FWHM}}$, obtained from the expression for the spectral intensity in Equation 2.14.

However it is also important to note how the presence of the chirp parameter can alter all the characteristics of the Gaussian Pulse. The new complex envelope will therefore be

$$\mathcal{A}(t) = \mathcal{A}_0 e^{\left(-\frac{t^2}{\tau^2}\right)} e^{\left(\frac{iat^2}{\tau^2}\right)} \tag{2.19}$$

where a is the chirp parameter from Equation 2.16.

In general, for the wavelength regimes studied in this project and for common transparent optical materials in this regime, the transmission of a short laser pulse through a medium will lead to its properties being altered. One change is the stretching of the pulse to a duration longer than the Fourier Transform Limit (FTL), caused by the chirping of the pulse as it propagates through the material. The FTL is the shortest pulse duration obtained when the phase is flat and when there is a chirped phase, the duration increases. This chirp refers to different frequencies of the pulse spectrum arriving at different times. In practice a common optical element to compensate for the chirp gained in a medium are chirped mirrors (CM). These are mirrors that transmit the electric field without conducting, meaning they have different path lengths for the different frequencies. This leads to all the different frequencies that had arrived at different times to converge back together. Propagation through a medium will induce a positive chirp while the chirped mirrors provide a negative chirp when bringing all frequencies together. These optical elements maintain the spectral width of the pulse constant but affect the pulse duration by shortening it. This phenomenon is further explained in the following section.

2.2.1 Dispersion and Pulse Propagation

As an electromagnetic wave travels through a certain medium it interacts with the different atoms and electrons. Throughout the path, these electrons will then be displaced and dipoles will be formed. By gathering all the dipoles, the medium will then pick up a polarization density $\vec{\mathcal{P}}$ dependent on the incident electromagnetic wave.

$$\vec{\mathcal{P}}(t) = \epsilon_0 \chi^{(1)} \vec{\mathcal{E}}(t) \tag{2.20}$$

where $\vec{\mathcal{E}}$ represents the electric field.

Equation 2.20 also shows a dependency on vacuum permittivity ϵ_0 and susceptibility χ. The latter is related to the refractive index of the material and represents the strength constant needed to form a dipole. Their relation is given by Equation 2.21.

$$n = \sqrt{1+\chi} \tag{2.21}$$

If the refractive index is dependent on the wavelength, implying that the susceptibility is too, then the medium is called *dispersive*. This is then shown by adding a spectral phase to the incident wave, given by Equation 2.22, where k is the wavenumber ($k = 2\pi n/\lambda$) and z is the medium length.

$$\phi_{\text{material}}(\lambda) = kn(\lambda)z \tag{2.22}$$

This can also be expanded to a Taylor Series around the central wavelength (λ_0)

$$\phi(\lambda) = \phi_0 + \frac{d\phi}{d\lambda}(\lambda-\lambda_0) + \frac{1}{2}\frac{d^2\phi}{d\lambda^2}(\lambda-\lambda_0)^2 + \frac{1}{6}\frac{d^3\phi}{d\lambda^3}(\lambda-\lambda_0)^3 + ... \tag{2.23}$$

where the second term represents the group delay (GD), the third term is the group delay dispersion (GDD) and the fourth term represents the third order dispersion (TOD).

In the normal dispersion regime, a dispersive medium is used to broaden a pulse because since there is a wavelength dependent refractive index $n(\lambda)$ and $v = c/n(\lambda)$, the different wavelengths will travel at different velocities. The shorter wavelengths (blue) travel slower than the longer wavelengths (red).

There are many types of dispersion depending on the origins of the condition [19], however for this project the specific types of dispersion of interest are material dispersion and nonlinear dispersion. Material dispersion arises from the wavelength dependence of the index of refraction or the absorption coefficient of the optical medium. This type is present when the laser beam propagates through a certain medium, and the different frequencies of the pulse spectrum travel at different group velocities arriving at different times. One clear example where material dispersion is present is when propagating white light through a prism. White light contains all frequencies and since the refractive index of the prism depends on each frequency value, they will arrive at different times thus leading to the separation of all wavelengths.

On the other hand, nonlinear dispersion is quite crucial when reshaping intense ultrashort pulses. This is because the nonlinear optical effects taking place are wavelength dependent, for instance self-phase modulation, which will be explained in further detail in the coming sections.

2.2.2 Few-cycle Regime

Laser pulses can be observed as packets carrying information on the electromagnetic field. As can be observed in the left sketch of Figure 2.4, the outer limitation of the packet, or so-called *envelope*, is the modulus of the amplitude of the electric field. This information, as mentioned previously, is the temporal contribution which gives the actual "length" of the pulse in time.

On the other hand, the inner part of the envelope is given by the real contribution of the electric field. The envelope thus wraps around the different cycles of the electric field. These oscillations of the field also travel inside the packet. There exists a relationship between the fast speed of the oscillations (carrier) and the slow speed of the pulse envelope, known as the *Carrier-Envelope Offset Phase*.

The pulse duration is related to the number of optical cycles per pulse by $N = \Delta\tau/T_0 = \nu_0\Delta\tau$, where T_0 is the period of the pulse carrier frequency ν_0. Pulses where the value of N is 1-3 are known as the "few-cycle regime" and normally occur for laser pulses with durations below 10 fs for near-infrared light. These laser pulses have shown great importance in applications such as attosecond science [4] and high-field physics [20]. The limit of few-cycle regime is achieved when there is a single oscillation in the carrier, a regime known as single-cycle. For a laser with central wavelength $\lambda_0 = 1030$ nm, the single-cycle regime corresponds to a pulse duration of 3.4 fs.

Few-cycle pulses are also a technique for increasing the peak power of a laser pulse. The expression is $P_{\text{peak}} = E/\tau$, where E represents the pulse energy and τ is the pulse duration. Therefore, by maintaining the energy constant and reducing the time duration, the peak power will increase.

The optical setup in this thesis has as an objective to generate few-cycle pulses by propagating the laser through a medium where nonlinearities are added as well as dispersion. The generation of new frequencies to increase the spectral content of the pulse is achieved by the interplay of both. Dispersion, as mentioned in the previous section, implies that different wavelengths will travel at different velocities, thus delaying them with respect to each other. For few-cycle pulses, dispersion and phase variation have a bigger impact than for longer pulses. Ultrashort pulses already have a very broad spectrum and thus any addition of new frequencies will lead to distortions of the pulse in the form of asymmetric pulses or pre- and post-pulses. An offset in the CEP will also vary the electric field of the pulse packet. Because the effect is much larger on these pulses, it is crucial to control the dispersion and phase variation by compensating for all possible orders of dispersion (Equation 2.23) and flattening the phase (equivalently, compensating for added chirp through dispersive elements such as chirped mirrors).

2.3 Non-linear Optics

One of the many ways to classify the broad field that is optics is depending on the interaction between light and matter. This provides a division into linear optics and nonlinear optics, where the behavior depends on the strength of the intensity of the incoming light. For low intensities, the interaction will be linear and thus the outcome will follow the electric field of the incoming light. However, for high incoming light intensities, namely those from a laser pulse, light and matter can interact nonlinearly. Nonlinear phenomena will appear when the material through which the light is traveling reacts in a nonlinear manner with respect to the electric field of the light. For instance, this can lead to frequency mixing effects.

The main differences between both sub-fields arise when studying the polarization, with its expression being:

$$\mathcal{P}(t) = \epsilon_0\chi^{(1)}\mathcal{E}(t) + \epsilon_0\chi^{(2)}\mathcal{E}(t)^2 + \epsilon_0\chi^{(3)}\mathcal{E}(t)^3 + ... \tag{2.24}$$

The first term is the special case of linear polarization. Additionally ϵ_0 is the electrical permittivity in vacuum and $\chi^{(1)}$ is the linear susceptibility, a material constant. For the cases when there is a stronger electric field, it is necessary to expand the first term, leading to the higher order values $\mathcal{P}_{NL}(t) = \epsilon_0\chi^{(2)}\mathcal{E}(t)^2 + \epsilon_0\chi^{(3)}\mathcal{E}(t)^3 + ...$

The nonlinearities are represented through the polarization because if the polarization varies new components of the electric field arise changing the expression for the wave equation as follows:

$$\nabla^2\mathcal{E} - \frac{1}{c^2}\frac{\partial^2}{\partial t^2}\mathcal{E} = \frac{1}{\epsilon_0 c^2}\frac{\partial^2\mathcal{P}}{\partial t^2} \tag{2.25}$$

When the second order susceptibility $\chi^{(2)}$ is nonzero then it is possible to do Three Wave Mixing. A particular example of this is Second Order Harmonic Generation (SHG). A material with strong $\chi^{(3)}$ response will exhibit Four Wave Mixing effects (such as Third Order Harmonic Generation (THG)) but also intensity dependent nonlinear effects such as Self-Phase Modulation (SPM) and Self-Focusing (SF) that, unlike the others, do not require phase matching.

SHG is a particular example of Three Wave Mixing characterized by both incoming light waves having the same frequency ω and generating an outcoming wave with doubled-frequency 2ω. This process occurs in non-centrosymmetric optical media such as Beta-Barium Borate (BBO) crystal (Figure 2.6). For this project, SHG is implemented in the pulse characterization step. Further information regarding this is given in the final section of this chapter.

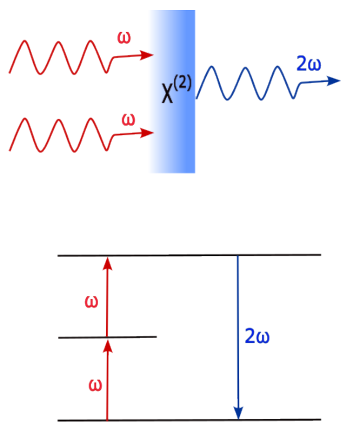

Figure 2.6: Second Harmonic Generation (SHG)

2.3.1 Optical Kerr Effect

From the third order nonlinear contribution to the polarization in Equation 2.24, we can observe that the polarization expression for the fundamental frequency ω leads to a variation in the susceptibility $\Delta\chi$:

$$\epsilon_0 \Delta\chi = \frac{\mathcal{P}_{NL}(\omega)}{\mathcal{E}(\omega)} = 3\chi^{(3)}|\mathcal{E}(\omega)|^2 = 6\chi^{(3)}\eta I \tag{2.26}$$

where $I = \frac{|\mathcal{E}(\omega)|^2}{2\eta}$ is the optical intensity of the incoming wave.

Recalling the relation between the refractive index and susceptibility $n^2 = 1 + \chi$ it is possible to derive the expression $2n\Delta n = \Delta\chi$ which then leads to

$$\Delta n = \frac{3\eta}{\epsilon_0 n}\chi^{(3)} I = n_2 I \tag{2.27}$$

with n_2 being the Optical Kerr Effect coefficient. A conclusion from this effect is that the refractive index is proportional to the intensity of the light as expressed in Equation 2.28.

$$n(I) = n + n_2 I(t, r) \tag{2.28}$$

where n_2 represents the nonlinear refractive index of the Kerr medium.

Since the laser pulse has a time-varying intensity, this will cause a time-varying refractive index (Equation 2.28) and thus leading to a time-dependent phase ($\Delta\varphi = -n_2 I(t) k_0 z$) and a new instantaneous frequency, computed by the time derivative of the pulse phase ($\Delta\omega_i = d\Delta\varphi/dt$). The very final result in the pulse will be a broader spectrum, an effect called self-phase modulation (SPM) (Figure 2.7 (top)). This concept introduces a chirp as well as the changes for the spectral content of the pulse. The case where the result is a broader spectrum occurs when the initial pulse is unchirped (a $=$ 0) or up-chirped (a $>$ 0). If the initial pulse is down-chirped (a $<$ 0) the result could even be a narrower spectrum.

A different result of an intense beam traveling through dispersive media, specifically Kerr media, is self-focusing (Figure 2.7 (bottom)). This is given when an intense beam propagates through the medium and changes the refractive index in such a way that it will be able to focus the light. The refractive index also becomes spatially dependent. Then, a Gaussian intensity profile will experience a refractive index gradient similar to a lens. If the beam width is w and peak power P then it is possible to express the focal length of this lens as

$$f_{kerr} = \frac{\pi \mathrm{w}^4}{8 n_2 d P} \tag{2.29}$$

where d is the thickness of the material through which the beam travels.

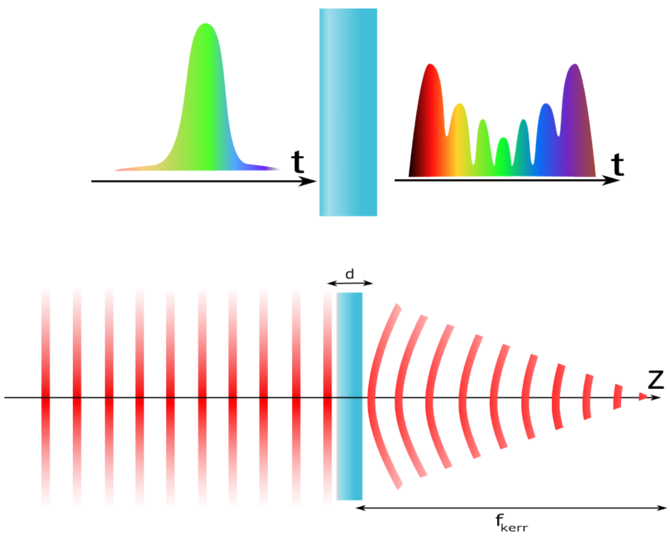

Figure 2.7: Self-phase modulation (top) and Self-focusing (bottom). For the top image, an incoming pulse with a narrow spectrum is broadened into a wide spectrum while adding a phase shift from the propagation. For the bottom image, the wavefront of a laser beam is represented as the red lines. The incoming beam has a planar wavefront and after the propagation through the Kerr medium acting as a thin lens, the wavefront is curved.

As observed, the refractive index variation depends on the magnitude of the intensity. The intensity of a Gaussian beam is stronger towards the center, so the effect of self-focusing will also be much stronger at the center than towards the wings of the beam. This entails smaller foci holding more intensity at the center. If propagation continues further, this effect will just cascade, eventually leading to damage of the material and strong degradation of the beam profile. Another consequence of this effect is that the curvature of the wavefront is altered, as can be seen in Figure 2.7 (bottom).

Regarding some limitations of these effects inside an MPC, the main restriction is the peak power of the laser pulse. High peak powers can entail damage of the bulk material because the ionization threshold has been reached. Also, at high peak powers there could be some beam degradation from the self focusing, and the mode of the beam traveling inside the cell can be unmatched because of extra lensing in the nonlinear optical element and thus affecting the nonlinear media and the cavity mirrors.

Both self-phase modulation and self-focusing occur together, simply the former is in the temporal domain while the latter is in the spatial domain. In order to measure the non-linear phase shift of light added due to these phenomena the B-integral is defined at the beam center as

$$B(r=0) = \frac{2\pi}{\lambda}\int_0^L n_2(z)I(z)dz \tag{2.30}$$

where L is the length of the nonlinear medium and I is the intensity along the optical axis. In the case of bulk MPCs this value is normally kept below $\pi/5$ per pass [21], although it is possible to achieve much higher values when using nonlinear mode matching [22]. When working with Gaussian pulses, the B-integral can also be related to the widths of the spectrum before ($\Delta\nu_{in}$) and after ($\Delta\nu_{out}$) the propagation

$$\frac{\Delta\nu_{out}}{\Delta\nu_{in}} = \sqrt{1+\frac{4}{3\sqrt{3}}B^2} \tag{2.31}$$

Equation 2.31 [12] is valid to use when the cause for the nonlinear phase shift is the Optical Kerr Effect coming from bulk or gaseous media.

2.4 Post-compression Techniques

Ultrafast physics makes use of few-cycle light pulses that additionally have high-energy. These pulses can be achieved through two different methods [23]: post-compression techniques or a variation of *Chirped Pulse Amplification* (CPA) [6], called OPCPA *Optical Parametric Chirped Pulse Amplification* [24]. Without going into too much detail, OPCPA consists of applying the CPA technique on an optical parametric amplifier. This method provides many advantages on the gain media, enlarging its bandwidth and also improving the quantum efficiency, beam quality and peak powers. Additionally, it also induces a gain through a single pass in a nonlinear medium, thus avoiding complex multipass geometries. Nonetheless, it comes with complicated synchronizations between pump and seed as well as detailed phase-matching issues. This also affects the conversion efficiency, providing very poor results in the range 10% and 20 %.

Therefore to overcome some of these trade-offs from OPCPA, post compression techniques offer a wide variety optimal for different necessities. Figure 2.8 shows the post-compression principle. Firstly, a pulse with a narrow spectrum but long time duration is sent through a Kerr medium, where its spectrum will be broadened due to self-phase modulation (through the MPC). Additionally, if we consider the initial pulse to have a flat spectral phase (dashed line in Figure 2.8), after its propagation through the gas or bulk material, it will gain a quadratic phase. Once with the broader spectrum and quadratic phase, the pulse is compressed in time (through the chirped mirrors) as close to the FTL where the outcoming pulse has a short time duration (broad spectrum), flat phase and high peak power.

The principle of post-compression is the same for all the possible techniques: in waveguides or through free space propagation.

Some advantages of post-compression through waveguides include maintaining a constant beam size and high intensity value throughout the propagation, thus allowing a high accumulation of the B-integral providing extensive spectral broadening. Also travel through a waveguide involves many

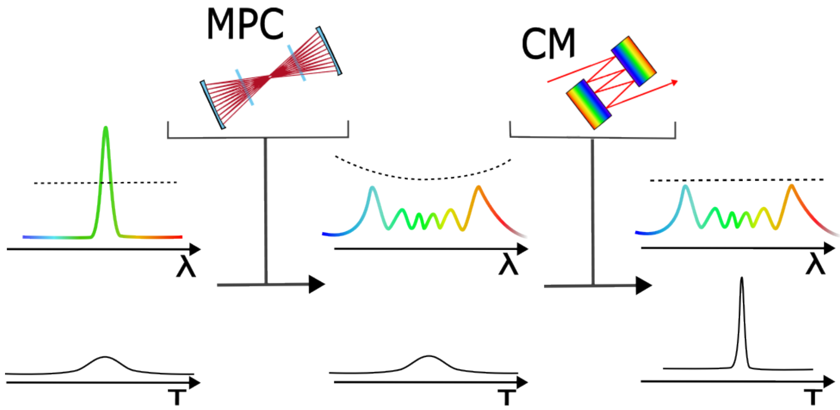

Figure 2.8: Post-compression Principle. An initial narrow spectrum is broadened through an MPC leading to a broader spectrum with quadratic chirp, which is flattened through a pair of chirped mirrors (CM).

reflections of the light, which makes it possible to mix the different parts of the beam giving rise to all the eigenmodes traveling together. This technique is carried out in practice through fibers with a solid core [25] or gas-filled HCF [9]. A drawback from waveguide use for post compression is the long lengths that they require, making it inadequate for compact setups and also they are quite complex to align.

On the other hand, spectral broadening through free space propagation can be achieved in solid-state systems such as a multi-plate continuum system, bulk filaments or through a multi-pass cell. All these make up quite simple and effective setups for post-compression. Nonetheless some trade-offs include inhomogeneous B-integral accumulation per pass and lower peak powers of the pulse in order to prevent the beam from collapsing. A positive note is that these problems can be diminished if an approach is taken where the nonlinear propagation is accounted for separately. Some free-space post-compression approaches make use of self-focusing which, as explained above, comes with self-phase modulation. For instance, in a multi-plate continuum system [26] the laser beam is focused just before the first bulk plate and then diverges only to be refocused by the following bulk plate, and so on iteratively. This approach has already shown a large compression factor of an Ytterbium laser system providing single-cycle duration pulses in the outcome [27]. The disadvantages expressed before are quite present for this setup, insinuating the power of the laser pulses must be several magnitudes larger than the critical power in order to obtain spectral broadening from a bulk medium, as it requires a higher B-integral. However, operating at values much higher than the critical power can lead to damaging of elements and even beam collapse. Spatial chirp is also a re-occurring issue in this setup as the bulk plates must be set at Brewster angle to reduce the reflection losses.

To decrease the high B-integral value that is piled up from each bulk plate in the multi-plate continuum system, MPCs were introduced for post-compression purposes. The difference is that the laser beam is focused between both mirrors, providing the same spectral broadening but with a smaller B-integral due to the several passes that allow a distribution of the nonlinearity. Therefore the lower B-integral values arise from the multiple passes inside the system. MPCs can also be built where the Kerr medium is a gas instead of bulk plates, thus providing a more continuous build up of the spectral broadening.

This leads to fewer losses due to the lack of optical interfaces to propagate through and nonlinear material damage. The major advantage from this technique include its power efficiency. However, bulk MPCs have a larger nonlinear refractive index than gases. This entails a shorter interaction length between the medium and the laser beam is required to achieve the same nonlinear phase shift, leading to much more compact setups. In addition to this, for bulk situations there is no need to include vacuum chambers.

However, as explained before post-compression not only involves generating a broader spectrum but it also requires flattening the phase that has become quadratically chirped from the SPM. By removing this dispersion the outcoming pulse will actually be compressed. This step can be done in one of two ways: chirped mirrors or a grating compressor. Both methods have the same goal, which is to induce a negative chirp in order to compensate for the positive dispersion from the incoming pulse.

Chirped mirrors [28] are built with specific coating layers for which the shorter wavelengths (blue) do not penetrate as far as the longer wavelengths (red) before being reflected. They normally possess a high reflectivity value and are characterized by having a central wavelength and bandwidth. Grating compressors [29] on the other hand require a more elaborate setup as they are made up of two gratings. The first will disperse the beam which will then travel towards the second grating and finally a retro-reflector which will send all the colors along the same path but in opposite directions and thus with the opposite chirp. Grating compressors also allow one to tune the duration of the outcoming pulse by changing the separation of both gratings.

Self-compression is also a possibility that has been experimented on in the past, consisting of the laser pulse being recompressed while it is being spectrally broadened and so completely skips the compression stage at the end. This is carried out by having chirped mirrors making up the cavity compensating for the GDD that is gained by the propagation through the Kerr media. This style of mirrors are the ones implemented in this project, compensating for the FS plates that are located in the center. Nevertheless, they will not be sufficient and so a compression stage will be needed at the end. Therefore, this MPC will not be considered to be inside the *Self-compression Regime*. Many studies have however been carried out successfully in this regime. Gröbmeyer et al. [30] achieved a compression to 31 fs from an initial 300 fs by exploiting the exact dispersion management of the MPC mirror and rendering a total efficiency of 85%. Another study making use of dispersion-controlling cavity mirrors was carried out by Silletti et al. [31] through a single stage gas MPC obtaining the compression of pulses with energies up 250 μJ with durations of 150 fs down to sub-20 fs time durations.

2.5 Ultrashort Pulse Characterization

Pulse characterization is the process of fully understanding and describing a laser pulse and is carried out through several studies: spectral, temporal, spatial, energetic and phase. As pulses keep getting shorter and shorter, their temporal characterization becomes more challenging due to the limited electronics. Detectors that are normally used for their diagnosis have response times in the microsecond scale, which is very slow compared to the pulses we wish to measure. Therefore in order to be able to measure these short time durations it is necessary to compare the duration with something on a similar time scale, in other words, compare the pulse with itself.

Spectral characterization involves measuring the intensity distribution of the laser pulse as a function of the wavelength by using a spectrometer. This information is crucial for this project as it shows the bandwidth of the pulse and, more specifically, the spectral broadening achieved through SPM. Additionally, this information is relevant for some temporal techniques. By taking the FTL, it provides a lower bound of the possible pulse duration.

Energetic characterization consists of measuring the pulse energy. This is actually calculated through the average power of the pulse (taken with a power-meter) and with the repetition rate of the laser system: $E = P_{\text{avg}}/R_{\text{rep}}$. In this project this is also a crucial parameter due to the presence of nonlinear effects and the importance of critical power.

As seen in the section for Ultrafast Optics, a pulse is defined not only by its intensity, but also by a phase, which will determine the shape in time. As mentioned, ideal Gaussian pulses are considered to have a flat-phase and pulse durations close to FTL. But after propagation through media, the phase will be altered affecting also the shape and duration of the pulse. Therefore it is crucial to measure, especially in the case of ultrashort pulses since the slightest variations will make the largest changes. The phase is measured with the same techniques as for temporal characterization.

2.5.1 Temporal Pulse Characterization

The way ultrashort pulses are measured in time is through nonlinear optical signal, with techniques such as autocorrelation [32], Frequency Resolved Optical Gating (FROG) [33] and dispersion-scan (D-Scan) [34]. This is another reason why ultrafast nonlinear optics is important, as it not only generates the pulses but it allows their own characterization.

Autocorrelation measures ultrashort laser pulses by firstly splitting the pulse into two exact replicas. One of them is then delayed in time with respect to the other and then both are finally overlapped inside a nonlinear crystal to achieve 3-wave mixing and SHG. By then varying the

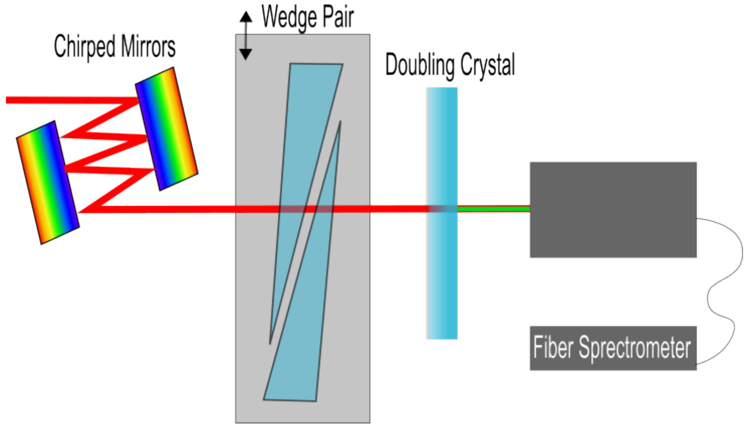

Figure 2.9: Typical D-Scan Implementation

delay between both pulses, the intensity of the second harmonic will vary providing an intensity correlation trace. The width of this trace will be an estimation of the pulse width in time. Some drawbacks from this include a prior assumption of the shape of the pulse, usually Gaussian, and there is no information regarding the phase of the pulse. As mentioned above, for longer pulses, the phase is not as decisive but once in the few-cycle regime it is crucial to have information regarding it.

FROG is defined as a spectrally resolved autocorrelation technique, therefore its principle is the same as above. The difference arises when the signal that is measured is actually gated and analyzed spectrally as a function of the delay. And so the rendered trace will be a spectrogram relating the wavelength as a function of the delay between pulses. The added information this provides is about the phase of the pulse. The exact extraction of phase information is also achieved through an iterative process where an initial assumption is made and fitted to the actual phase and repeated until obtaining a minimal error. This technique was used to measure the pulse duration for the laser system as well as the first stage MPC.

D-Scan (Figure 2.9), on the other hand, relies on modifications of the spectral phase through implementations of dispersion to the pulse. Some known dispersion is applied to the pulse by optical elements (wedges or prisms, for example). These are built on stages in order to control the amount of dispersion added to the pulse. As the pulse travels, a varying dispersion is applied to the pulse. Then this pulse generates a nonlinear signal through SHG and finally, the spectrum of the nonlinear signal is recorded as a function of the dispersion added. The signal is then mapped as a trace of the GDD versus the second harmonic signal and through numerical algorithms the temporal profile and phase are extracted. The pulse duration is then deduced from them. The specific apparatus [35] used for this project was a certain implementation using a grating-based pulse stretcher-compressor pair. The use of gratings as dispersive elements leads to larger amounts of dispersion being applied, which allows to characterize pulses with a larger range of pulse durations.

2.5.2 Spatial Characterization

Spatial characterization refers to observing the beam and studying its shape and size, as well as the divergence. This is done by taking M^2 measurements, which tell us how close the beam is to a perfect Gaussian ($M^2 = 1$) as well as how small and aberration free the spot size can be. It also gives information on the divergence of the beam, for instance high values of M^2 indicate low beam quality and fast divergence.

One important parameter is the *Beam Parameter Product* (BPP) defined as the product of the beam waist radius (w_0) and the beam divergence half-angle (θ):

$$BPP = \mathrm{w}_0\theta \tag{2.32}$$

The BPP of a perfect Gaussian beam can be written as $BPP_{\text{ideal}} = \lambda/\pi$. Therefore, since the goal is to compare the beam quality to that of a Gaussian, the definition of the M^2 parameter is given by:

$$M^2 = \frac{\pi\theta\mathrm{w}_0}{\lambda} \tag{2.33}$$

Studying Equation 2.33, it is possible to see it is a dimensionless parameter, where higher values ($>$1) state worse beam quality and values closer to 1 represent better beam quality. This study is crucial because, once this factor has been defined, it is possible to plug it into the mathematical equations of the general Gaussian beam to acquire a more specific representation.

Experimentally, the measurement is done by taking images of the beam profiles through the focus. Therefore it is important to start with a collimated beam and focus it with a lens. Then several images are acquired before and after the location of the focus. From these images, the beam diameter is extracted for each and plotted adding a hyperbolic fit on both the X-axis (position from the focus) and Y-axis (beam diameter). Finally from the fit it is possible to extract the beam divergence half-angle, the beam waist and the M^2 value.

Chapter 3

Multi-pass cell (MPC)

Multi-pass cells have been around for quite some years although just recently [36] have been introduced as one of the post-compression techniques. An MPC is made up of two curved mirrors positioned in front of each other in between which the beam can travel back and forth several times passing as well through a Kerr medium (Figure 1.1). They are sturdy constructions that provide large amounts of nonlinear phase shift from all the roundtrips inside the cell. The principle behind the MPC is mainly based on self-phase modulation inside the nonlinear medium which can be gaseous or bulk (glass plates). With every pass inside the cell there is an added nonlinear phase modulation to the pulses that increases the B-integral of the system providing bandwidth gain. The chirp that is induced to the pulse from this nonlinear medium is then removed by a compressor placed separately from the cell that will give the compressed laser pulse.

3.1 The Herriott Configuration

A Herriott-Type Cell [37] is made up of two concave mirrors of the same radius of curvature placed on the same axis and facing one another. The in-/out-coupling of the laser beam can be carried out by drilling a hole in one of the mirrors or by an in-/out-coupling mirror placed in the optical setup. Once inside, the laser beam then travels back and forth for the estimated number of roundtrips leaving an elliptical shape of the reflection pattern on each of the mirrors (Figure 3.1). The elliptical shape of the pattern is due to the nonparallel laser beam, with respect to the axis of the mirrors. It is necessary that the incoming beam is slightly off-axis and for a certain angle of the beam the Herriott pattern can be tuned to be circular.

The different reflection spots of the pattern are separated by an arc given by the angle between them. This angle advance ξ determines the re-entrant condition of the Herriott-Type MPC as is shown in Equation 3.1. In practice, the re-entrant conditions ensure that the laser beam that is out-coupled of the cell is the same as the beam that is being in-coupled.

$$\xi = \frac{2\pi k}{N} \tag{3.1}$$

where N is the number of roundtrips and k = 1, ..., N-1. The integer k helps determine the length of the cell.

$$C = \frac{L}{R} = 1 - cos(\xi/2) \tag{3.2}$$

where L and R define the cell length and radius of curvature of the mirrors, respectively.

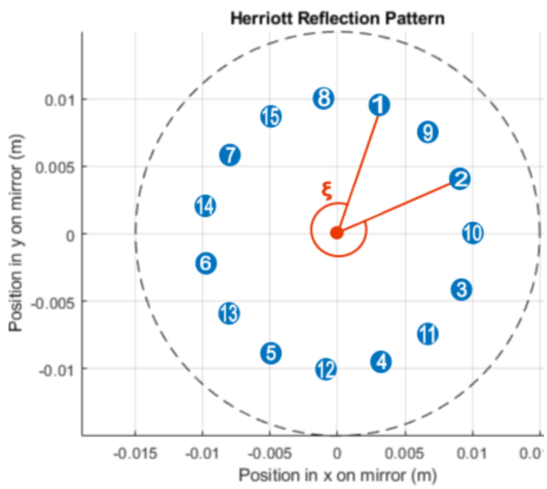

Figure 3.1: Herriott Pattern on one Cavity Mirror for N = 15 with Advance Angle for k = N-2

3.2 Beam Sizes

In the previous chapter it was mentioned how the MPC is considered a resonator, nonetheless it is important to mention that for pulse compression to take place nonlinear propagation must occur. But, in the remaining aspects it can be compared to a stable optical resonator, thus with linear propagation. In these cases the beam that is traveling back and forth is the eigenmode, which happens to be the Gaussian beam, with its specific beam waist w_0 and radius $R(z)$. When bringing this concept into the nonlinear propagation it is important to set the eigenmode before entering the cavity, to avoid losses. As the beam comes far from the cavity eigenmode, there will be some power loss after the propagation since some parts of the beam will not be supported by the cavity. Additionally, it ensures that the eigenmode of the laser beam maintains its size. This is carried out by a process called *Mode-matching* and is experimentally done with a detuned telescope. The focus is set to be in the center of the cell and the curvature of the beam propagating every roundtrip is matched to the curvature of the cell mirrors. These specific parameters (from [12]) for the Herriott MPC are given by

$$\mathrm{w}_0^2 = \frac{R\lambda}{2\pi}\sqrt{C(2-C)} \tag{3.3}$$

$$\mathrm{w}_m^2 = \frac{2\lambda}{\pi}\sqrt{\frac{C}{2-C}} \tag{3.4}$$

Equation 3.3 shows the focal spot radius and Equation 3.4, the radius of the beam on the mirrors. Mode-matching ensures stability of the size on the mirrors as well as a clean beam profile, preventing distortions and clipping.

This can be observed in Figure 3.2, where the variation of the beam size along the propagation inside the cell is simulated. The horizontal axis represents the number of passes (half a roundtrip). Each pass essentially represents a mirror of the cavity, therefore at these positions the beam size is the maximum value, given by Equation 3.4. Between each pass, there is a dip in the size of the beam and this is the focus through which the beam propagated each time. The size of the beam at the focus is then given by Equation 3.3. The graph shows the change in beam size for different incoming energies into the cell, where it is possible to observe an extremely small ($\leq 20\mu$m range) change in beam size (both at the mirror locations and at the focus) for each energy. This plot was obtained by making use of the ABCD matrices in Table 2.1. A cavity was simulated with 2 fused silica bulk plates of thickness 1 mm separated by a distance of 170 mm. The cavity was built with two concave mirrors of radius of curvature 200 mm separated by a distance of 380 mm for 7 roundtrips (14 roundtrips), which will be the actual setup in the laboratory, although Figure 3.2 shows fewer for better visualization purposes.

Each pass was built as shown in Figure 3.3 where the matrices used were, respectively (Table 2.1): reflection from a curved mirror (M_R), propagation through distance x (M_x), transmission

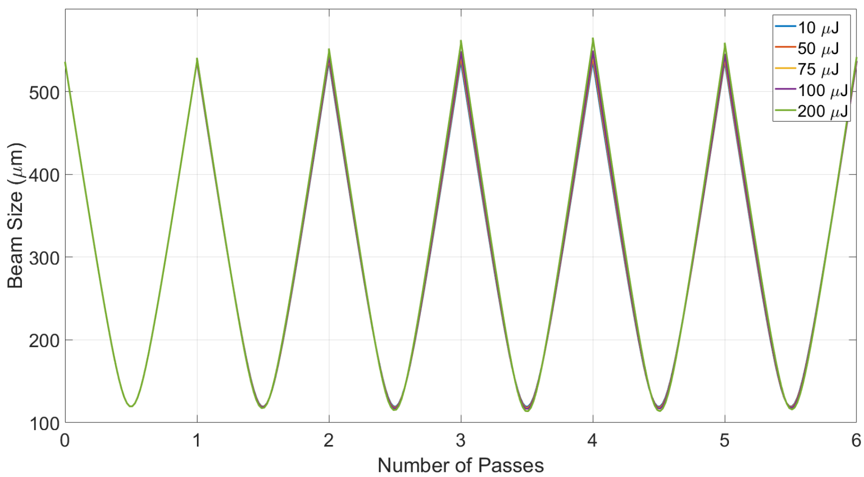

Figure 3.2: Variation of Beam Size in a Mode-matched Bulk MPC for different pulse energies

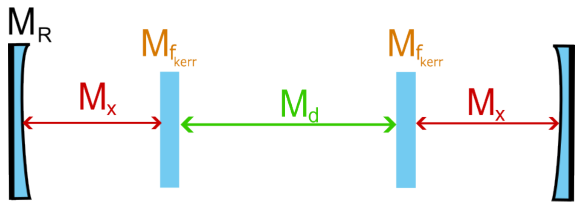

Figure 3.3: MPC Architecture Schematic for Beam Size Simulation

through a thin lens ($M_{f_{kerr}}$), propagation through distance d (M_d), transmission through a thin lens ($M_{f_{kerr}}$) and propagation through distance x (M_x).

It is also of great importance to know the limit of the maximum pulse energy the cell can resist as this value is typically the damage threshold of the optical elements making up the cell. How close the laser beam is to the *laser-induced damage threshold* (LIDT) can be measured through the fluence (Equation 3.5) and the experimental conditions. Surface LIDT depends on the material as well as coatings and, in the case of bulk materials, focusability and material quality also come into play.

The fluence and peak intensity are respectively defined as:

$$F = \frac{2E}{R\lambda}\sqrt{\frac{2-C}{C}} \tag{3.5}$$

$$I_0 = \frac{4P}{R\lambda}\frac{1}{\sqrt{C(2-C)}} \tag{3.6}$$

where E and P are the pulse energy and pulse peak power, respectively [12].

The peak intensity is another crucial parameter in the study of the limitations of the cell. Equation 3.6 shows the value of the intensity at the center of the cell and since the placement of the bulk plates is not in the center, but symmetrically placed from the center, then the peak intensity does not enhance the LIDT. In the case of gas-filled MPCs this will severely limit the scaling due to possible gas ionization. In the case of the bulk-MPC of this project, this factor conditions the possible air ionization setting an upper intensity bound for high pulse energies, although it is much weaker than in gas-filled MPCs. Additionally, Equation 2.30 shows how the B-integral is dependent on the intensity, therefore it will also limit the nonlinear phase accumulation. For high values of the intensity, distortions and breaking of the beam could take place. The peak intensity can also approach the critical power for self-focusing leading to beam collapse or hot spots, which are local damages.

Kerr lensing is quite influential on these parameters and will vary the spot sizes inside the cell, thus it is important to take into account when mode-matching [22]. For both gas and bulk MPCs there will be strong self-focusing, decreasing the spot size even more and so increasing the peak intensity values. Ionization is possible to take place for gas filled MPCs, where the Kerr medium can be altered chemically. Similarly, in bulk the operation takes place in the critical self-focusing regime scaling close to the LIDT.

3.3 Nonlinear Medium: Gas or Bulk

As mentioned in the previous section in order to obtain spectral broadening of the laser pulse through all the passes inside the cell it is crucial for there to be a Kerr Medium for self-phase modulation to take place. The nonlinear medium can be either gaseous or solid-state. Gaseous MPCs make use of rare gases (helium, neon, argon, etc.) and bulk MPCs usually have Fused Silica (FS) plates. The selection is down to the input peak power of the cell: above the megawatt range (1 MW = 10^6 W), gaseous media are used while below the gigawatt range (1 GW = 10^9 W), bulk media are typically used.

The main difference, in terms of the nonlinear phase shift added by gas or bulk media is the localization of the nonlinearity. As the gas is homogeneously spread inside the cell and there are no surfaces to travel through the spectral broadening takes place continuously. The nonlinearity steps are discrete with bulk plates. The latter, however allows the use of linear focusing optics in order to keep the B-integral low per pass.

Although the ranges of use for each medium are different, most bulk MPCs are still used at lower peak powers (10 to 100 MW). The reason the rare gas MPCs are not preferred now is due to the low nonlinearities they provide and their inability for large spectral broadening. Additionally, bulk MPCs provide a compact setup without the need to include vacuum chambers and gas equipment. Bulk MPCs are very attractive to measurements where power scaling is carried out because the nonlinear plates can be placed arbitrarily at locations of lower intensities. It is even possible to place several thin plates to increase the nonlinearities per pass but nonlinear mode-matching is crucial for this case to avoid damaging of the optical elements.

Nonlinearities in gas MPCs can be varied by changing parameters of the gas, such as pressure. It is important nonetheless to watch out for the scaling limits as high pulse energies can degrade the beam quality and efficiency of the cell. On the plus side, due to the lack of propagation through different interfaces the efficiency of gas MPCs is much higher, scaling usual efficiencies of 95%.

3.4 MPC for Few-cycle

The left sketch in Figure 2.4 shows a temporal representation of a laser pulse. It is made up of an envelope given by the amplitude of wavefunction and a carrier shown by the different optical cycles inside the envelope which are the real component of the wavefunction. An optical cycle can be defined as a complete oscillation of the electric field and is essentially the shortest pulse duration of a light wave. This duration is dependent on the wavelength.

The few-cycle regime gathers all laser pulses with 1-3 cycles inside the envelope. The duration will be greater for the longer wavelengths. For instance, the optical cycle duration for 800 nm, 1030 nm and 1500 nm will be 2.67 fs, 3.43 fs and 5 fs, respectively. The usual wavelength range for few-cycle pulse generation is in the long infrared regime, partly due to the lower dispersion for the nonlinear refractive index of the Kerr medium. Therefore this stores very short pulse durations which, by taking the Inverse Fourier Transform, translate to very large spectral broadening. This can sometimes pose as a challenge when it comes to their generation, in terms of the bandwidth supported by optical elements. For instance the limits of the used dielectric coatings of the cavity mirrors which are broadband 1030 nm with high efficiencies (99.99%) only support around 30 fs bandwidths. One possible fix to this issue involves metallic coatings on the mirrors. Metallic mirrors support more than two octaves of bandwidth for the usual wavelength range used. But they still come with some challenges. The first is related to the reflectivity (98% to 99%), which is notably lower than for dielectric coatings, where the reflectivity is practically total. This means that there is more light that is not being reflected from the mirrors and will be absorbed by them, leading to heat increase. Some methods for cooling, such as water cooling would then be necessary.

Post-compression of Ytterbium-based lasers is already very common using MPCs in the few-millijoule range and up to terawatt peak power values. The positive aspect of this technique, is that when it is desired to scale to higher pulse energies it is as simple as lengthening the setup taking into account the limitations of the cell: LIDT and ionization. But very high compression factors are obtainable by a combination of separate post-compression techniques, a method known as cascaded setups [38]. This allows optimizing efficiency and compression quality of the entire setup. For instance, in a double-stage system, the overall efficiency improves because the first stage can still be built with very high reflectivity dielectric mirrors. Müller et al. [16] carried this exact setup by cascading two gas-filled MPCs. The first stage cell was built with dielectric mirrors and rendered 31 fs pulses with a transmission of 95%. Then the second stage achieved a final output of 6.9 fs with a transmission of 85%. The second stage in this setup was built for fewer roundtrips in order to minimize the losses even more with each bounce on the metallic cavity mirrors, reducing as well the heat absorbed also through cooling.

Overall, few-cycle pulse generation has proven possible through this technique and the only limiting factor for the shortest pulse duration is to maintain the spectral broadening without mishandling the phase. In order to avoid this from happening when generating few-cycle pulses, the step carried out by the chirped mirrors in the compression stage was implemented as part of the cell. The cavity mirrors were swapped for dispersion-compensating mirrors. [17]. This is one possibility to achieve self-compression as mentioned previously, and also allows for even more compact setups, since the final compression stage is normally no longer needed. Some drawbacks include the damage threshold of the mirrors changing with every pass because of the iterative pulse duration and intensity variation with each roundtrip.

We considered all the previously mentioned aspects to design the post-compression setup. As the goal is to achieve few-cycle pulses, a cascade architecture will be needed made up of two bulk-based cells placed one after the other so that the outcoming pulse from the first stage is the incoming pulse into the second. The second stage however will not be a replica of the first since, as mentioned above, dispersion must be accounted for. A dispersion-managed cell will be implemented in the second step with dispersive cavity mirrors that will compensate for the dispersion accumulated from the bulk fused silica plates.

3.5 Cavity Dispersion Design

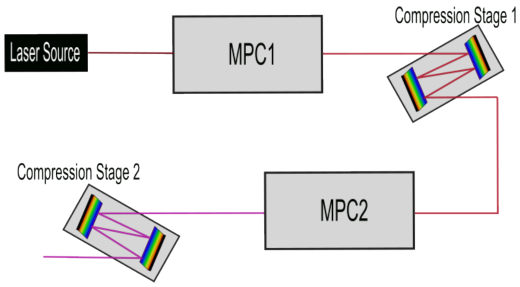

Figure 3.4: Schematic of Cascaded MPC System

The setup used in this project consists of exactly a cascade of 2 multi-pass cells: MPC 1 and MPC 2 (Figure 3.4). The second stage MPC (MPC 2) in this project was designed in a similar manner as the existing first stage (MPC 1) although considering the necessary changes to the dispersion: chirped cavity mirrors and uncoated FS plates.

The use of chirped mirrors allowed for compression of the pulses as they were being spectrally broadened. Specifically, the chirped mirrors (CM) used were paired mirrors that compensated for 3 mm of FS in the wavelength range 700 nm to 1400 nm. Figure 3.5 shows the precise compensation between the average of the GDD of the CM and the inverse sign of the GDD of 3 mm of FS. The mirrors were both concave with radii of curvature 200 mm each.

The second change to account for dispersion is related to the FS plates. There is no anti-reflection coating for such a broad targeted spectral width, corresponding to few-cycle pulses. Thus the fused silica plates are uncoated and placed at Brewster angle to minimize losses in the system.

The fact that the plates were placed at Brewster angle also relates to the dispersion because the propagation length varied. The amount of GDD from the bulk plates inside the cavity should come close to the GDD compensated by the paired mirrors of the cell. Although the FS plates were

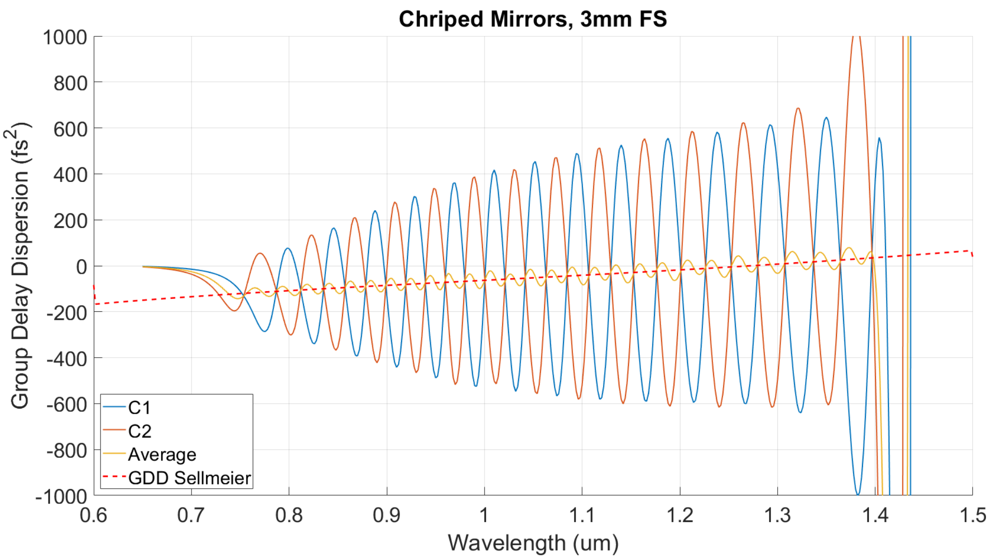

Figure 3.5: GDD of CM 1 and 2 as a function of the wavelength. The average GDD is shown in orange and compared to the opposite GDD of a 3 mm thick piece of Fused Silica (dashed red line) calculated from the Sellmeier equations. The cavity mirror data is extracted from the group delay obtained from the mirror manufacturer.

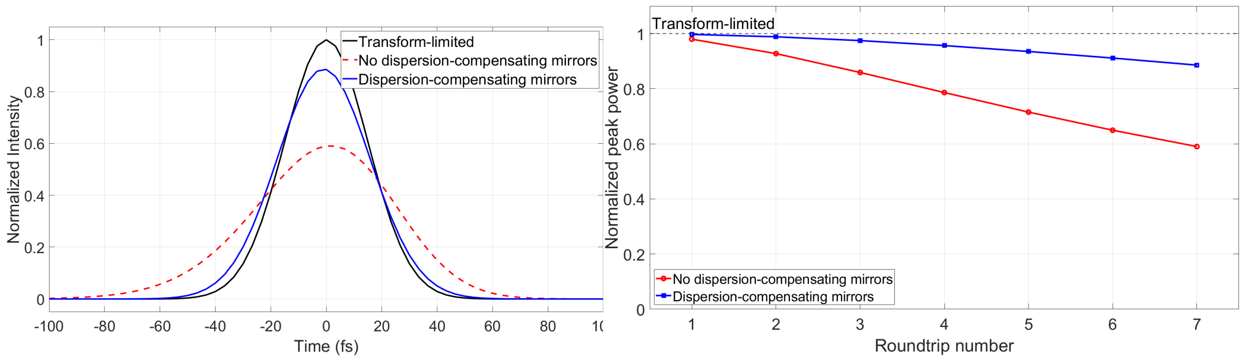

(a) Normalized Intensity vs Time **(b) Peak Power vs Roundtrips**

Figure 3.6: Simulated comparison between Dispersion-compensated Pulse and Non-dispersion-compensated Pulse. For the dispersion compensated scenario, paired CM compensating for the equivalent GDD to 3 mm were taken into account. For the non-dispersion compensated case, non-chirped mirrors were taken into account.

actually 1 mm thick, since they were placed at Brewster angle ($\theta_B = 55.41°$), this means the actual geometrical length traveled was 1.215 mm. And so, there is no longer much more overcompensation from the mirrors.

All these changes were necessary in order to achieve larger nonlinearities and therefore spectral broadening. Had dispersion compensation been neglected then with the constant change of pulse duration and intensity within each roundtrip, SPM would not had been possible. In this case, the GDD would keep accumulating after each roundtrip of the pulse through the cell, leading to a stretched pulse in time. In this case there would only be dispersion from SPM which would then accumulate with each propagation through the plates resulting in a loss of peak intensity as the pulse stretches in time and suffers losses. Figure 3.6a shows this simulation where the transform-limited, dispersion compensated and non-dispersion compensated cases are compared. The transform-limited plot represents the theoretical Fourier transform of a Gaussian spectrum, with FWHM 50 fs, in this case neither GDD nor SPM were taken into account, and are used as a comparison reference. The case with dispersion-compensated mirrors was built as the planned setup for the project: 2 paired CM mirrors compensating for 3 mm of FS GDD and 2 FS plates with thickness 1 mm placed at Brewster angle (actual propagation length 1.2 mm). The plotted pulse is the final outcome after 7 roundtrips in such cell, where after each roundtrip the GDD is being compensated for but the SPM is being accumulated, explaining the slight decrease in intensity compared to the FTL. Lastly, the non-dispersion compensated case was built in a similar manner as above, but with normal curved mirrors for the cell, rather than chirped mirrors. The plot also shows the final pulse after 7 roundtrips and the larger decrease in intensity is due to the constant accumulation of both GDD and SPM. The GDD stretched the pulse in time as well as decreasing the intensity, challenging the system to carry out SPM. Figure 3.6b shows the step-decrease of the peak power for each roundtrip in both cases as well. Should the number of roundtrips have been more, at some point the peak intensity would have been below the value for self-focusing and SPM would have been quite weak.

One final feature was also taken into account when calculating the dimensions of the cell. In order to reduce the losses as much as possible a lower number of roundtrips was needed, so that the reflection losses at the mirrors and plates was fewer. But it was still important to have enough to achieve sufficient spectral broadening through SPM. Therefore the chosen amount of roundtrips was N = 7 and, using the radius of curvature of the cell mirrors and Equation 3.2, the chosen cell length was L = 38 cm.

The parameters related to the re-entrant condition (Equation 3.1) have been chosen to satisfy the stability and thus k = N - 1. However for different values of k there is a wider range of possibilities for the cell length, as is shown in Figure 3.7. This graph provides the different cell lengths (reaching a maximum of N = 7) for the different values that the k-parameter can reach (k = 1, ..., N-1) and also showing the different values of the angle advance from the re-entrant condition (Equation 3.1).

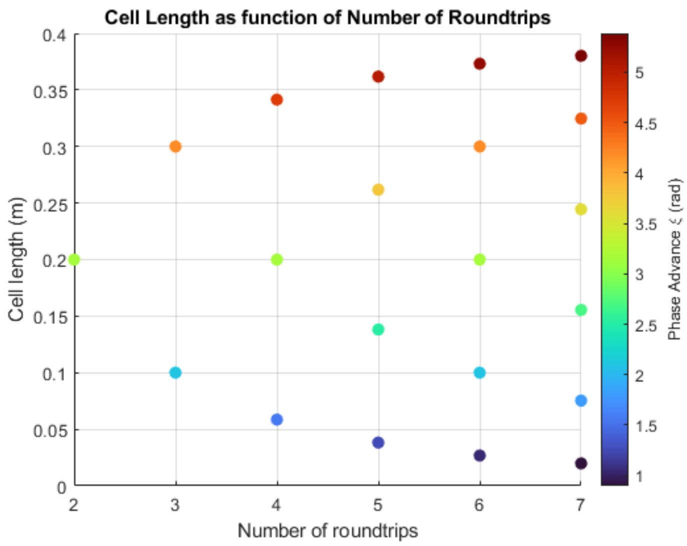

Figure 3.7: Cell Length as a function of Number of Roundtrips (for a maximum of N = 7 and R = 200 mm)

3.5.1 Analysis of Nonlinear Propagation Simulations

In order to simulate the propagation of the laser beam through the MPC the propagation equation must be studied. The SISYFOS [39] code, created by G. Arisholm models nonlinear optical propagation, such as parametric processes and, in our case, spectral broadening. Therefore, using this written code, I analyzed the results of interest for our experimental setup. This code is of interest when simulating MPCs as it accepts quite broad bandwidths in the spectrum, which is what is occurring through SPM in the cell. The input parameters into the simulation must be those of interest when building the cell: radius of curvature of the mirrors and the distance that separates them, the incoming pulse duration and energy and finally, the desired beam size on the mirrors. The nonlinear media can also be considered, thus in the case of this thesis, two fused silica plates separated by a certain distance. The number of roundtrips is also a simulation parameter.

The parameters used for the simulations analyzed are shown in Table 3.1. It is important to mention that the simulations run are not calibrated, therefore will provide some differences with respect to the calibrated results and also the experimental results. Nonetheless, they provide an expectation for the outcome.

Parameter	Symbol	Value
Cavity Mirrors Radius of Curvature	ROC	200 mm
Cell Length	L	380 mm
Number of Roundtrips	N	7
Thickness of FS Plates	d	2 x 1.2 mm
Separation between FS Plates	z	280 mm
Input Pulse Duration	τ_{in}	50 fs
Input Pulse Energy	E_{in}	70 μJ
Input Electric Field	$\mathcal{E}$	Perfect Gaussian
Beam Size on Mirrors	w_m	535 μm

Table 3.1: SISYFOS Simulation Parameters

The code provides the FTL of the outcoming pulse (8.4 fs) as well as the maximal peak irradiance (571.3 GW/cm^2).We can extract the temporal profile of the pulse before and after the cell, as well as the spectrum, both are shown in Figure 3.8.

Additionally, it also represents the spectral broadening depending on the propagation length in terms of roundtrips. Figure 3.9 shows the simulated broadening of the input spectrum of the laser pulse as a function of the number of roundtrips, showing the increase of the bandwidth for more passes through the nonlinear media. This provides a base for what we can expect to obtain.

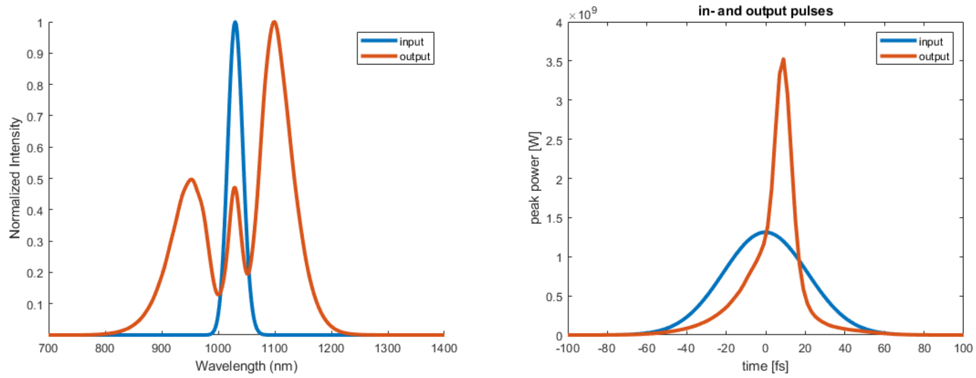

(a) Intensity vs Wavelength

(b) Peak Power vs Time

Figure 3.8: MPC 2 Output vs Input for an incoming pulse of 50 fs duration and 70 μJ energy. The output pulse duration is 8.4 fs.

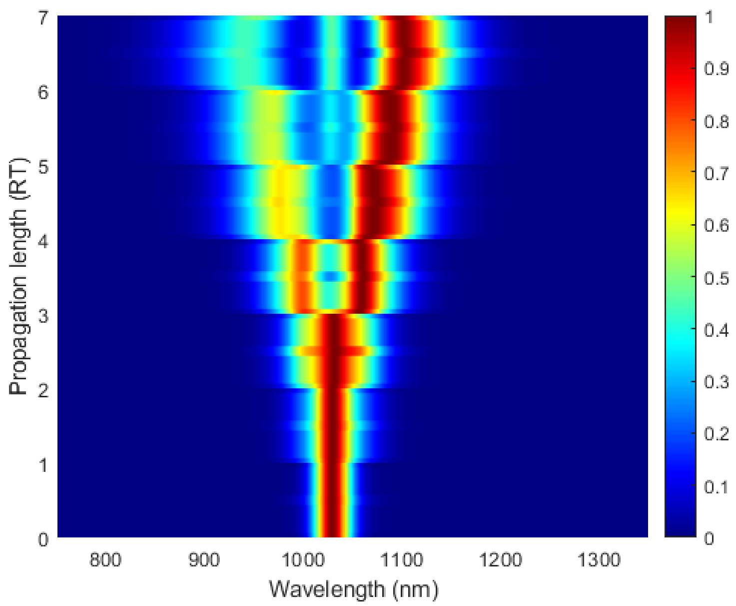

Figure 3.9: Simulation of Spectral Broadening in MPC 2 as a function of the Propagation Length (in Roundtrips). The side color bar represents the normalized spectral evolution

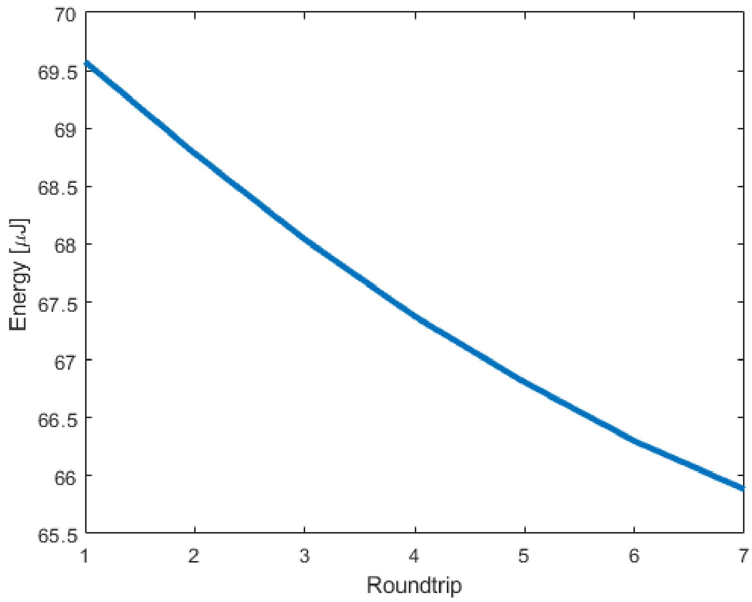

Figure 3.10: Simulation of Pulse Energy after Different Roundtrips

Another quite interesting outcome shows the dependency of the pulse energy on the number of roundtrips, Figure 3.10. Here it is possible to observe the remaining energy of each pulse at each roundtrip, since there will be losses for each pass in the cell. However in this graph it is possible to notice the lack of calibration as it states that the total transmission of the cell will be 95% when in reality it will be much lower. This is due to the fact that losses of the plates are not fully accounted for in the simulations and that a perfect Gaussian input beam was used for the simulations.

Chapter 4

Experimental Setup & Results

4.1 The Laser Source

For this experiment, the light source in use was an industrial-grade solid-state Ytterbium amplified laser system (Carbide, Light Conversion). The operating parameters are presented in Table 4.1. Figure 4.1 also shows the spectrum of the laser. This laser system comes with a tunable repetition rate which allows changes in the average power. It also has a built-in attenuator in the laser box which allows to change the output pulse energy.

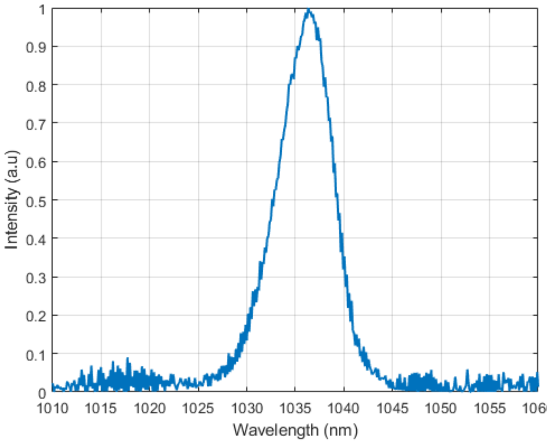

Figure 4.1: Laser Spectrum

Parameter	Symbol	Value
Central wavelength	λ_0	1036 nm
Bandwidth (FWHM)	$\Delta\nu$	6.38 nm
Pulse duration (FWHM)	τ	219.7 fs
Average Power	P	80 W
Repetition rate	R_{rep}	40 kHz
Pulse energy	E	2 mJ

Table 4.1: Laser system parameters.

It is also possible to estimate the maximum peak power of the laser pulse by taking the ratio of the pulse energy divided by the pulse duration considering also a factor for the Gaussian pulses.

$$P_{\max} = 0.94 \cdot \frac{E}{\Delta t} = 9.09\text{GW} \tag{4.1}$$

For the experimental work in the lab the normal laser settings involved a repetition rate of 8 kHz and the pulse energy was dropped to approximately 100 μJ.

4.2 MPC 1

The first step to achieve the goal of this project is to build the cascade of multi-pass cells. This allows the outcoming pulses of the first stage to be the incoming pulses for the new second MPC. The first stage MPC (MPC 1) (similar to setups in [15] and [40]) is also a Herriott MPC made up of two focusing mirrors making up the optical resonator. In between are placed the bulk plates acting as Kerr media to achieve the progressive spectral broadening with every pass through SPM. Alongside the spectral broadening, the pulse also acquires a phase, normally quadratic, which will then need to be compensated for with the compression stage. The laser beam enters the cell through an in-coupling mirror which satisfies the Herriott re-entrant condition (Equation 3.1). The passage through the cell will leave the characteristic circular pattern on the mirrors and after the laser beam will exit the cell through the same in-coupling mirror, acting now as the out-coupling mirror. As mentioned previously, the beam traveling through the cell must be the eigenmode, achieved with a mode-matching telescope placed before. This ensures that the beam size on the mirrors remains constant for all roundtrips. The peak power takes values above the critical power for self-focusing in order to have substantial nonlinear response and thus spectral broadening via SPM, and depending on its peak power value the mode-matching is adjusted. Nevertheless, it is important not to exceed very high values to avoid beam collapse.

The experimental setup is shown in Figure 4.2 and the parameters are given in Table 4.2. Right after the laser output there is an attenuator that controls the input energy into the setup. This attenuator is made up of a half-wave plate and a thin-film polarizer. Normally the input energy into MPC 1 for this experiment is 100 μJ. The following is the mode-matching telescope, consisting of a diverging lens followed by a converging lens. The cell is made up of two concave mirrors with a radius of curvature (ROC) 300 mm. The cell is built for 11 roundtrips, thus has a length of 49.6 cm. The fused silica plates, with 1 mm thick anti-reflection coating, are placed symmetrically around the center separated by a distance of 280 mm. After coupling out from the cell the laser beam is collimated by a curved mirror (M3) with ROC 1500 mm sending it to the compression stage. This final step consists of two chirped mirrors compensating for the SPM quadratic phase and the propagation through the fused silica plates.

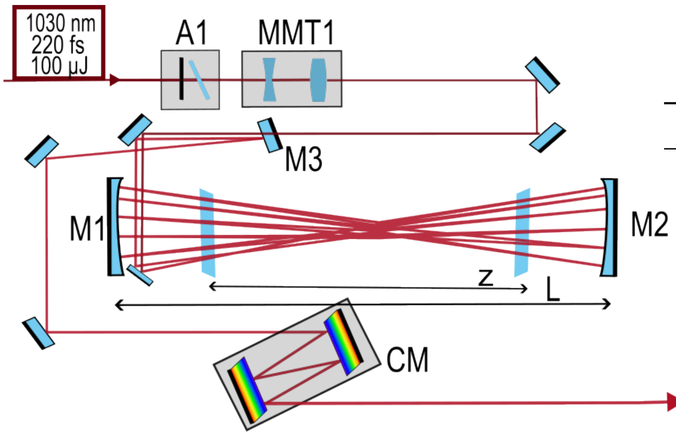

Figure 4.2: MPC 1 Experimental Setup. A1: Attenuation Stage. MMT1: Mode-matching Telescope. M1 and M2: MPC Cavity Mirrors. M3: Collimating Curved Mirror. CM: Chirped Mirrors (Compression Stage)

Parameter	Symbol	Value
Mirrors Radius of Curvature	M1, M2	300 mm
Cell Length	L	496 mm
Number of Roundtrips	N	11
Nonlinear Material	FS	2 x 1 mm
Separation between FS Plates	z	280 mm
Input Pulse Duration	τ_{in}	220 fs
Output Pulse Duration	τ_{out}	50 fs
Input Pulse Energy	E_{in}	100 μJ
Peak Power	P	1.88 GW

Table 4.2: MPC 1 Parameters

The transmission of the cell of MPC 1 is 86%, while the transmission after the chirped mirrors is approximately 80%. After out-coupling from the cell there is a compression stage made up of 2 chirped mirrors that compensate for the GDD gained through the spectral broadening. One mirror compensates for -200 fs^2 while the other, -1000 fs^2. The total compensation is -2400 fs^2 obtained by 2 bounces on each mirror.

Figures 4.3 show the retrieved output spectrum and the retrieved temporal profile of MPC 1 used for the duration of the project as the input into MPC 2. These measurements were taken with a FROG.

In Figure 4.3a the spectrum for MPC 1 is plotted as a function of wavelength. The spectrum of the laser system is also overlapped in order to show the spectral broadening gained from SPM. Considering the central wavelength is 1036 nm, it is possible to say that the broadening is quite symmetric towards the red and blue. The new bandwidth of the pulse is $\Delta\nu_{out} = 47.37$ nm. The phase of the pulse is quite flat which is also visible when comparing the pulse duration of the pulse (50 fs) (Figure 4.3b) with its FTL (48.6 fs), which are very similar.

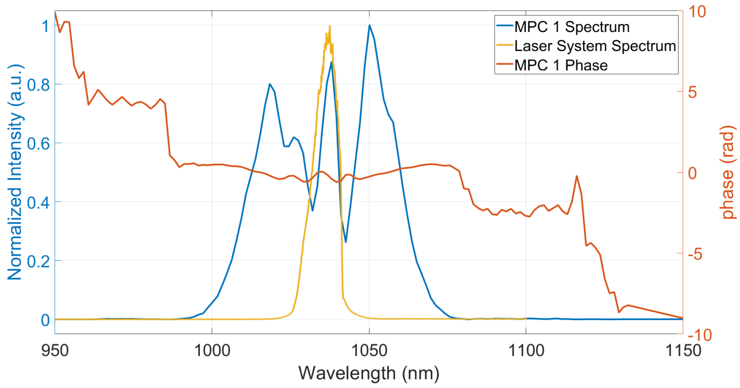

(a) Pulse Intensity (left axis) and Phase (right axis) as a function of Wavelength

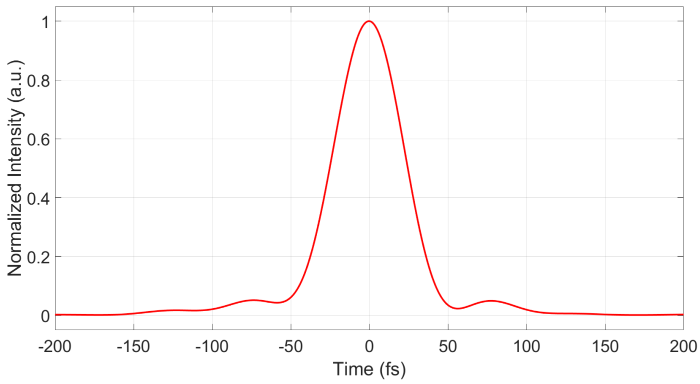

(b) Pulse Intensity as a function of Time

Figure 4.3: MPC 1 Result for Incoming Pulse with duration 220 fs and energy E = 100 μJ. The Output Pulse Duration is 50 fs.

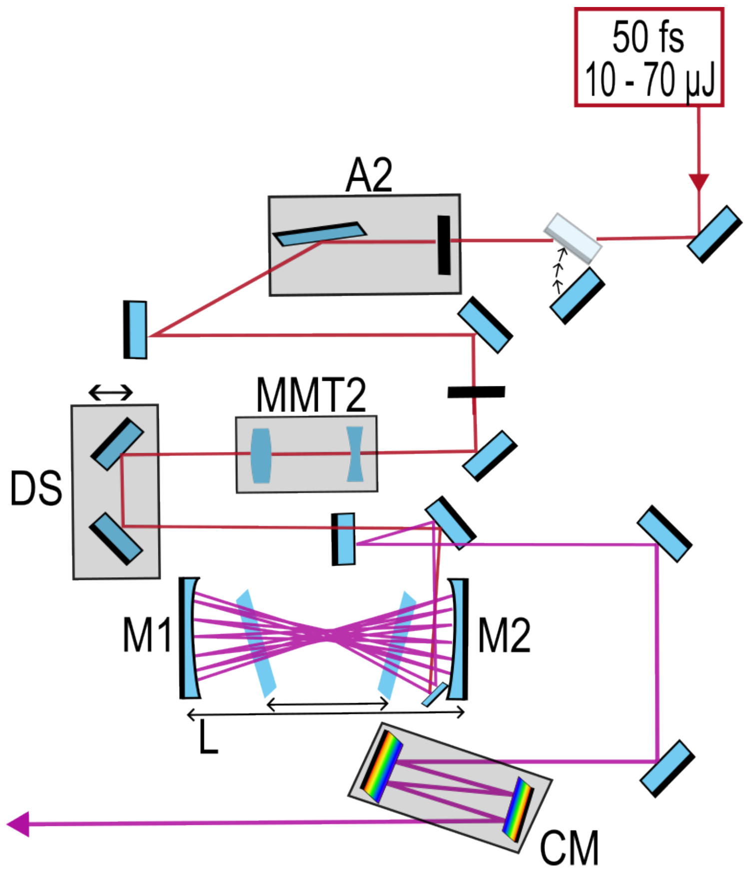

Figure 4.4: MPC 2 Experimental Setup. A2: Attenuation Stage. MMT2: Mode-matching Telescope. M1 and M2: Dispersion Compensating Cavity Mirrors. DS: Delay Stage. CM: Chirped Mirror Compression Stage

4.3 MPC 2

Parameter	Symbol	Value
Mirrors Radius of Curvature	ROC	200 mm
Cell Length	L	380 mm
Number of Roundtrips	N	7
Nonlinear Material	FS	2 x 1.215 mm
Input Pulse Duration	τ_{in}	50 fs
Input Pulse Energy	E_{in}	10 - 70 μJ
Mode-matching Telescope	f1, f2	-100 mm, 200 mm
Focus Size	w_0	110 μm
Beam Size on Mirrors	w_m	536 μm

Table 4.3: MPC 2 Parameters

Once the design and calculations for MPC 2 had been established we proceeded to its building. The experimental setup is shown in Figure 4.4 with the corresponding parameters in Table 4.3. The laser beam comes from the output of MPC 1, where we have first placed a flip mirror which is added when characterization of the first stage is carried out. Immediately after there is an attenuation stage made up by a wave plate and thin film polarizer in order to control the pulse energy input of MPC 2. The input pulse energy into the second stage has varied as it was of interest to study the outcome depending on it. The range of energies was kept between 10 μJ and 70 μJ, approximately. The beam was then guided towards the mode-matching telescope. The diverging lens with focal length f_1 = -100 mm and converging lens of focal length f_2 = 200 mm are separated by a distance of approximately 190 mm. Nevertheless, as the diverging lens is placed on a stage, it is possible to alter this distance, which is also useful when aligning MPC 2 further on. The focus was placed approximately 118 cm from the converging lens and had a focus size radius of 110 μm. To find the precise position of the focus, a delay stage was implemented to be able to tune this distance whenever the mode-matching telescope was slightly tuned when aligning. The beam continued towards the metallic in-coupling mirror and into the cell. The cell is also a concave-concave setup where the radii of the mirrors are 200 mm. The mirrors of that make up the cavity (M1, M2) are paired chirped mirrors that compensate for the equivalent GDD gained through the propagation in 3 mm of FS. It is built for 7 roundtrips, as specified in the previous chapter, therefore a cell length of L = 38 cm, which also falls inside the stability range for resonators (L≤2R). The fused silica plates in the cell were no longer coated and therefore placed at Brewster angle, where the propagation thickness increased from 1 mm to 1.215 mm. The plates were initially set at an arbitrary separation, which will also be a parameter to be studied. After the stipulated number of roundtrips the beam is out-coupled through the same coupling mirror and directed towards the compression stage. The transmission of MPC 2 is approximately 65%. The chirped mirrors used for compression were the same type as the cavity mirrors, although flat rather than curved. They were also paired CM compensating for 3 mm of FS per pair of bounces. Once compressed the laser pulse is guided towards the characterization step done by the dispersion-scan apparatus, which also required further attenuation done with wedges.

4.3.1 Spectral Broadening Results

Following the order of building MPC 2, the first set of results involved measuring the spectral broadening obtained by the SPM inside the cell. These were taken before the compression stage had been included in the setup. They involve spectral measurements of the laser beam exiting the cell after 7 roundtrips. The goal was to visualize the spectral broadening induced from SPM from the propagation through 2 times 1.215 mm of FS (1 mm at Brewster angle θ_B = 55.41°). The separation between them was placed arbitrarily and then altered to observe the dependence of the spectral broadening on it.

The first set of measurements included constant input pulse energy at E = 25 μJ and different distance between the FS plates. The spectra were taken through an Optical Spectrum Analyzer (OSA) which accurately displays the power distribution of an optical source over a certain wavelength range. Figure 4.5a shows the spectral broadening for all cases. Some noise reduction has been carried out, however it is possible to observe the inverse dependence of the bandwidth with the separation of the nonlinear plates. In other words, the closer the plates are placed, the stronger

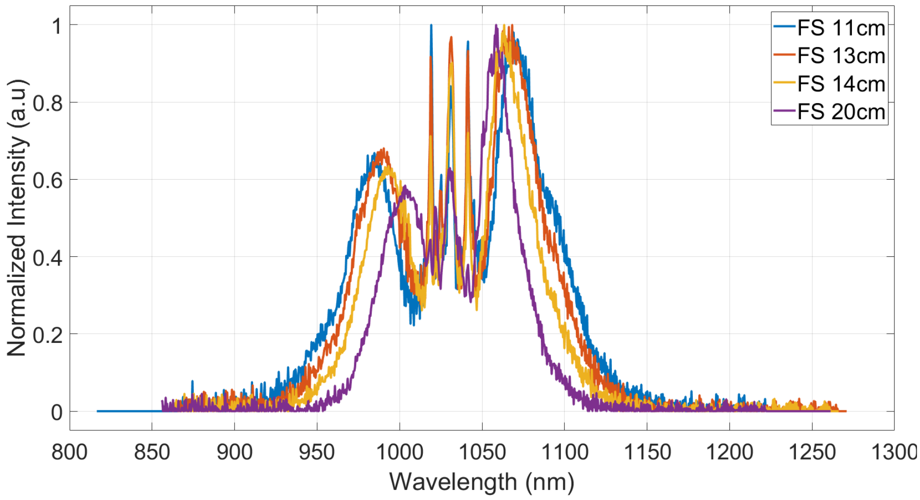

(a) Spectral Broadening from Self-Phase Modulation

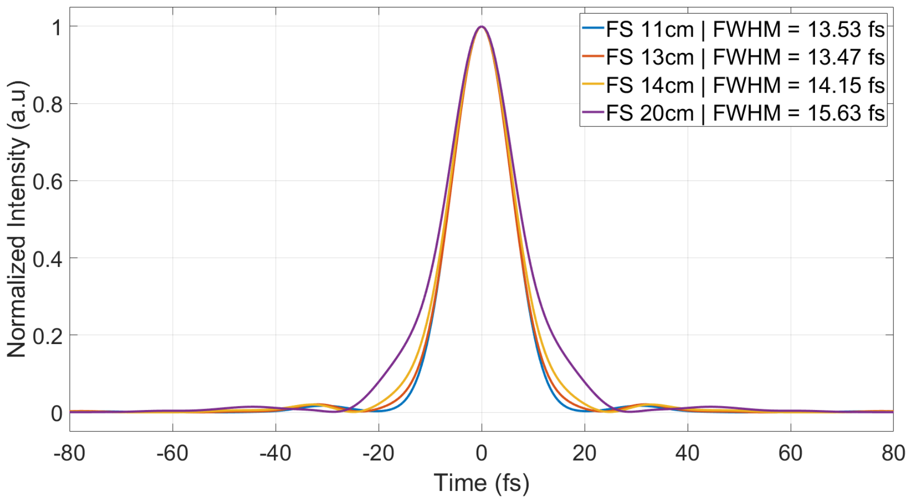

(b) Fourier Transform Limits from the Different Broadened Spectra above

Figure 4.5: Spectral Measurements of MPC 2 at E$_{in}$ = 25 μJ for different FS separation

the nonlinearity from SPM is. From these graphs it is possible to find the B-integral for the propagation of the beam through the cell, by using Equation 2.31. Since the pulse coming from MPC 1 had a duration of $\tau_{in} = 50$ fs and a spectral broadening of $\Delta\nu_{in} = 47.37$ nm and the bandwidth for the scenario of the FS plates at 11 cm is $\Delta\nu_{out} = 125.5$ nm, then the total value of the B-integral is 2.8 rad. As there have been 7 roundtrips (14 passes), this accounts for approximately 0.2 rad per pass, which is well below the limit of $\pi/5$ [21].

Similarly, when taking the FTL for each spectrum the shorter separations provide shorter theoretical pulse durations, as shown in Figure 4.5b. It is visible that the shortest supported pulse duration would be 13 fs.

The following step was to vary the energy. For three plate separations three energies were measured and the spectral broadening was observed. Figure 4.6 shows how strong the energy dependence on spectral broadening is. This matches with the theoretical prediction since the expression of the time-dependent phase occurring due to the Optical Kerr Effect is written as

$$\Delta\phi_{NL} = n_2 I(t) L_{eff} \tag{4.2}$$

where n_2, I(t) and L_{eff} represent the nonlinear refractive index, time-dependent pulse intensity and effective length of propagation, respectively. Thus by increasing the pulse energy for a constant plate separation, equivalently I(t), a larger phase shift will accumulate leading to a broader

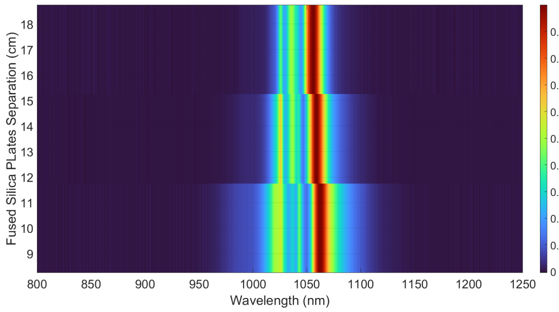

(a) E = 10 μJ

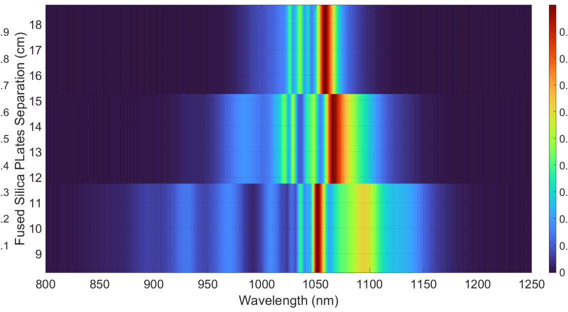

(b) E = 20 μJ

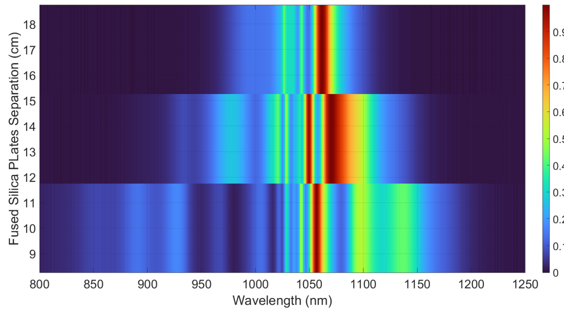

(c) E = 25 μJ

Figure 4.6: Spectral Broadening from SPM at different energies and FS plate separation

spectrum. As for the study of the variation of the plate distance, it is also related to the intensity in Equation 4.2. For a smaller distance there is a stronger focusing, thus self-focusing is much stronger. This will also increase peak intensity inside of the plates and with it $\Delta\phi_{NL}$.

A further observation of the spectra measured involves the homogeneity of the broadening. Figures 4.6 show a non-uniform distribution of the broadening to the left and right of the central wavelength in terms of intensity. This trails back to the discussion regarding the input pulse to MPC 2, where since the spectral phase is negative for the longer wavelengths the structure will be altered and the frequencies redistributed. The red components of the pulse arrive earlier in time and so the SPM is stronger for the lower frequencies.

4.3.2 Pulse Compression Results

The setup of MPC 2 continued with the implementation of the compression stage. With each pass through the FS plates, SPM adds new spectral bandwidth which is both intensity-dependent and time-varying. Positive GDD is also implemented which will stretch the pulse in time while accumulating nonlinear phase. The CM then apply negative GDD partially recompressing the pulse before the next pass. With this overcompensation the pulse entering the FS plate the next time will be shorter and with higher peak power, implying more SPM in the next phase. This overcompensation will then lead to a net negative GDD per roundtrip but it is still not self-compressed because the spectral phase acquired from SPM is not being canceled by the accumulated dispersive phase. In order to have self-compression, the total nonlinear phase would have to match the total negative GDD and the higher dispersion orders (TOD and FOD) would also need to be matched (the FS plates and the chirped mirrors have TOD but they do not cancel in the same way). Since these features are not taking place in the setup a compression stage is needed at the exit of the cell. This stage is composed of two similar chirped mirrors as the cavity mirrors but with a flat radius of curvature. This shows how our system is not inside of the self-compression regime, although close. The flat mirrors on the compression stage are also paired mirrors compensating for the GDD of 3 mm of FS.

The first set of measurements of the compressed pulse were taken for a plate separation of 10 cm. To start the observation of the remaining second order dispersion on the pulse, only one bounce on each chirped mirror was set. The pulse was then guided to the dispersion-scan including some wedges for intensity attenuation.

For two different input pulse energies the results are shown in Figures 4.7 and 4.8. For both Figures, the first row of plots ((a) and (b)) represent the measured and retrieved traces of the pulse being studied. These are built by measuring the spectrum at each insertion of the dispersion element inside the beam (values of the y axes). Then they are overlapped to obtain a 2D plot. The graph (c) in both sets of Figures shows the spectrum retrieved at 0 mm insertion, which represents the laser pulse directly at the entrance of the pulse characterization device. Therefore the actual pulse. Graphs (d) are the pulse retrievals at the 0 mm insertion, corresponding to the spectrum in (c). This plot gives information of the pulse shape and duration. Finally, graphs (e) and (f) are also the spectra and pulse retrieval, respectively, at 0 mm of dispersion insertion but for a specific virtual pulse propagation. The dispersion-scan retrieval algorithm software allows us to simulate propagation through certain materials in order to virtually compress a laser pulse. It is possible to add or remove materials or GDD/TOD/FOD to virtually optimize the laser pulse that is being measured to observe the outcome and potentially implement more adequate compression experimentally.

For the lowest energy the outcome is shown in Figure 4.7. Although the retrievals show some promising results as the noise is low and there is no sign of a pedestal, the retrieved pulse is very poor. If we first focus on the spectrum, it is possible to see broadening, however very inhomogeneous and the phase of the pulse is also quite quadratic. From this, it is possible to predict an unsatisfactory temporal shape. Nonetheless, by taking advantage of the feature to virtually propagate the pulse, optimization was carried out and it was observed that removing 10.8 mm of FS was needed to flatten the phase. This addition then provided a shaped pulse with a duration of 10.7 fs.

The same study was carried out for a second incoming pulse energy of 25 μJ. Initially, a similar outcome was observed. After some careful optimization, a short pulse of 9 fs was virtually obtained after virtually removing 8.9 mm of FS. From this study we concluded that further compensation of GDD was needed for the outcoming pulse as the phases were not yet flat.

For the continuation of the measurements the separation distance between plates was increased to 17 cm as it also allowed for higher energy variations. From the results shown in Figures 4.7 and 4.8 we concluded that more GDD needed to be accounted for, thus the number of bounces on the compression stage chirped mirrors was increased to 2 on each, giving a total of 4 bounces.

The results are shown in Figures 4.9 and 4.10. Firstly, Figure 4.9 represents a heat map of all the pulses retrieved. It provides a 2D representation of the normalized intensity of each pulse (provided by the color scale) as they are plotted in terms of time and the incoming pulse energy. The main outtake from this plot is the presence of several side pulses for each pulse. These are visible especially for higher input pulse energies and appear as bands with moderate intensity values. This tells us that the outcoming pulses are still not quite compressed to a single pulse, but still have a train leading to them. Additionally, studying the color scale, it is possible to observe that the pulses with medium energy have a stronger pulse intensity in their center.

Observing the same results from a different perspective, Figure 4.10 shows the pulse shapes for certain incoming energies. These plots provide a clearer representation of the shapes, in terms of the side pulses created. From the large difference in intensities between the measured pulses and the FTL, it is also clear that these pulses are not optimal. As it scales directly with the intensity, the phase shift will be larger and so the asymmetric phase will lead to this distortion in the pulse.

We look into the phase of each pulse. In terms of the higher-order dispersion, we found that, although the GDD was quite compensated, the TOD values were quite high. Making use of the feature on the dispersion-scan to simulate propagation through a certain medium, we virtually decreased the TOD contribution to the phase to optimize the pulse shape. The rendered pulses were much more satisfactory and it was seen that the amount of compensation for all energies was kept inside of the range (+ 0.8 kfs^3 and + 1 kfs^3).

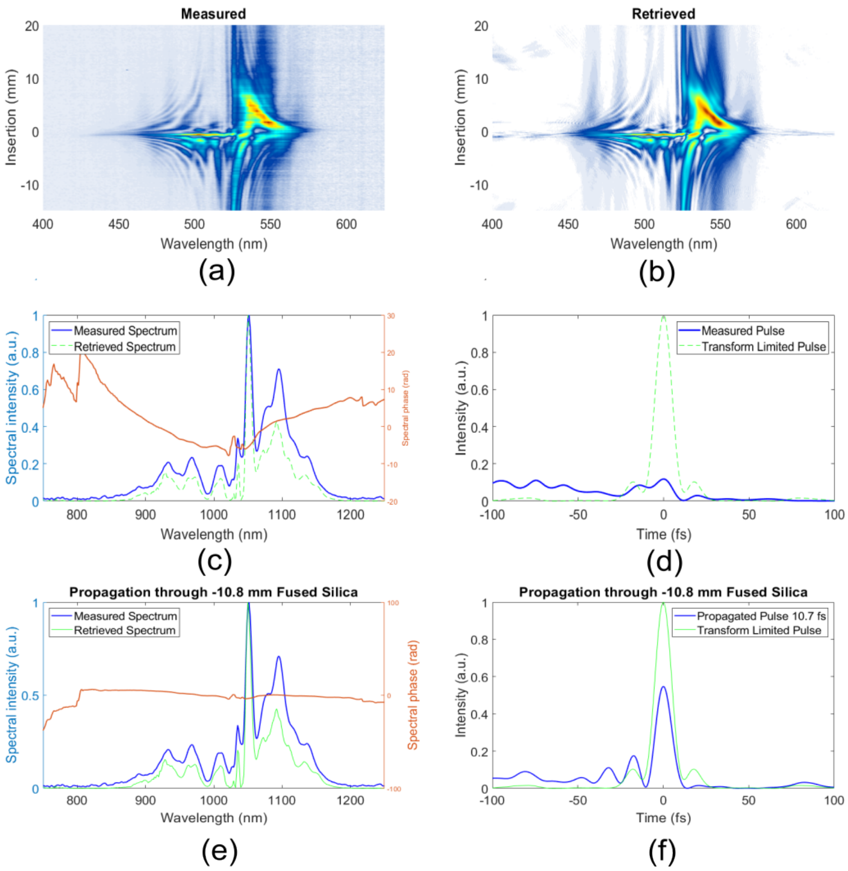

Figure 4.7: D-Scan Retrieval E$_{in}$ = 20 μJ FS Plates Separation 10 cm. (a) Measured laser beam map obtained by measuring the spectrum at each insertion of the dispersion elements into the beam path. (b) Retrieved laser beam map acquired after applying the software algorithm. (c) Spectrum of the laser beam for 0 mm insertion, representing no added dispersion. (d) Pulse retrieval corresponding to 0 mm of dispersion added. (e) Spectrum of the laser beam after virtual propagation through -10.8 mm of Fused Silica. (f) Pulse retrieval corresponding to spectrum after virtual propagation through -10.8 mm of Fused Silica compared to Transform Limited Pulse.

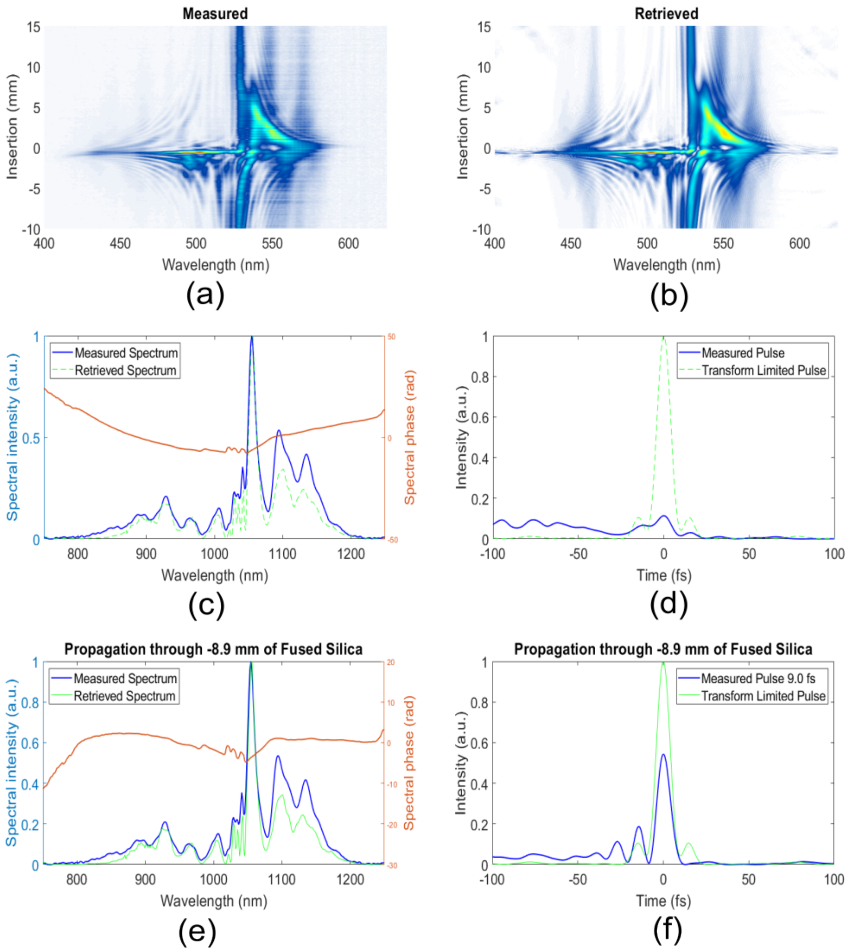

Figure 4.8: D-Scan Retrieval E_{in} = 25 μJ FS Plates Separation 10 cm. (a) Measured laser beam map obtained by measuring the spectrum at each insertion of the dispersion elements into the beam path. (b) Retrieved laser beam map acquired after applying the software algorithm. (c) Spectrum of the laser beam for 0 mm insertion, representing no added dispersion. (d) Pulse retrieval corresponding to 0 mm of dispersion added. (e) Spectrum of the laser beam after virtual propagation through -8.9 mm of Fused Silica. (f) Pulse retrieval corresponding to spectrum after virtual propagation through -8.9 mm of Fused Silica compared to Transform Limited Pulse.

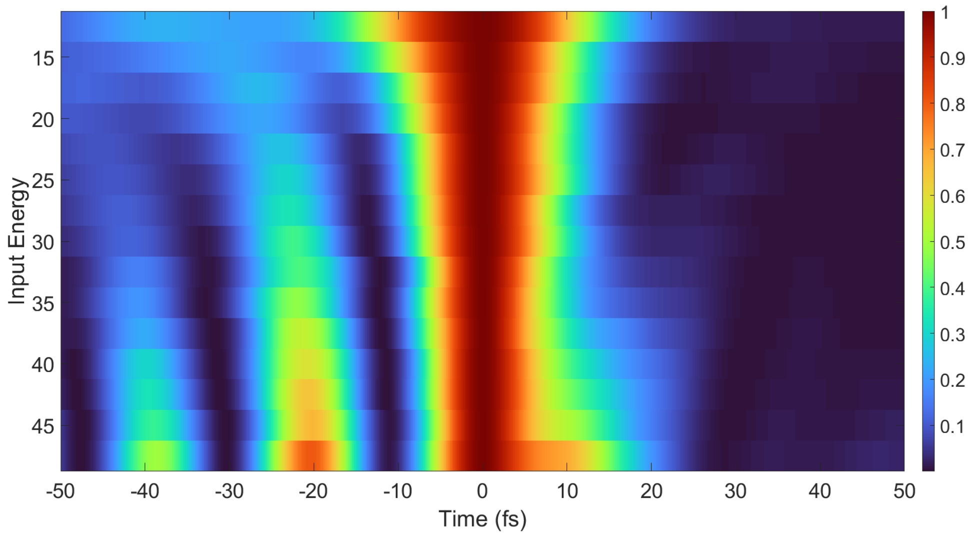

Figure 4.9: Pulse Shapes for various incoming pulse energies for FS plate separation of 17 cm. The graph was built by overlapping the pulse retrievals acquired at 0 mm insertion of dispersion elements (no dispersion) for different input pulse energies. The color scale represents the intensity normalized by the maximum intensity value of each pulse retrieval.

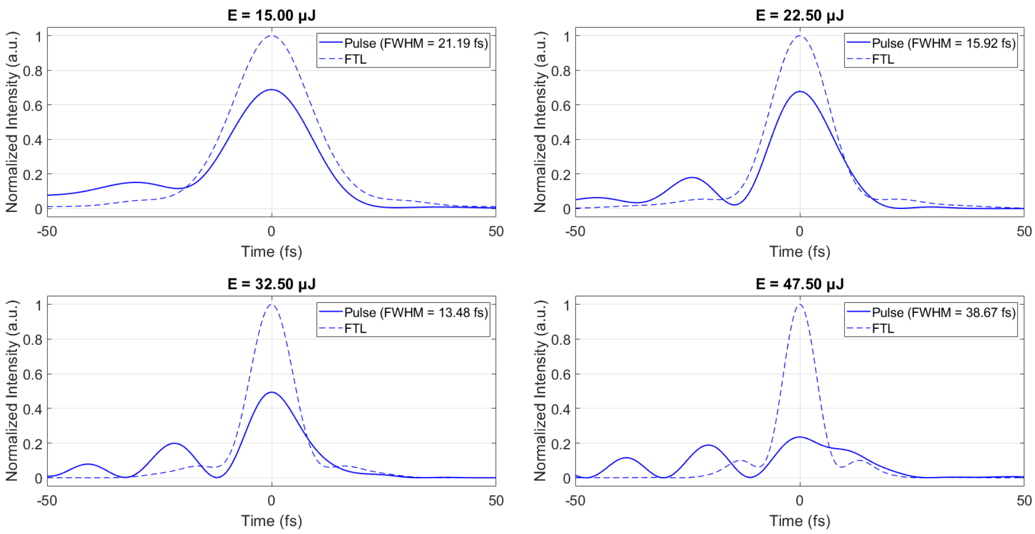

Figure 4.10: Pulse Shapes for certain incoming pulse energies for FS plate separation of 17 cm. The pulse retrievals were taken for 0 mm of dispersion insertion in the dispersion-scan.

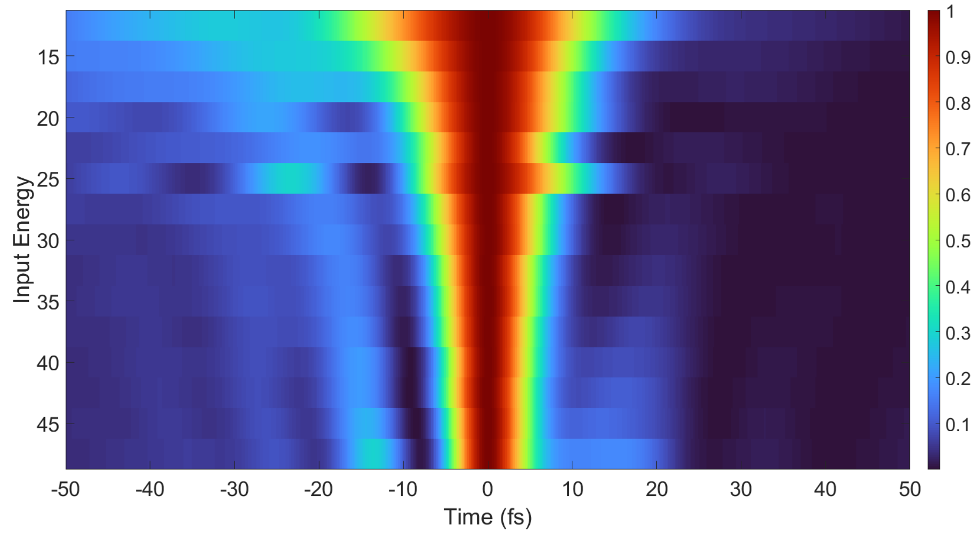

Figure 4.12: Pulse Shapes for various incoming pulse energies considering virtual propagation through 5 mm of KDP and 5 mm of FS. The graphs were obtained by overlapping the pulse retrievals acquired at 0 mm dispersion insertion for different input pulse energies. The color scale represents the intensity normalized by the maximum intensity value of each pulse retrieval.

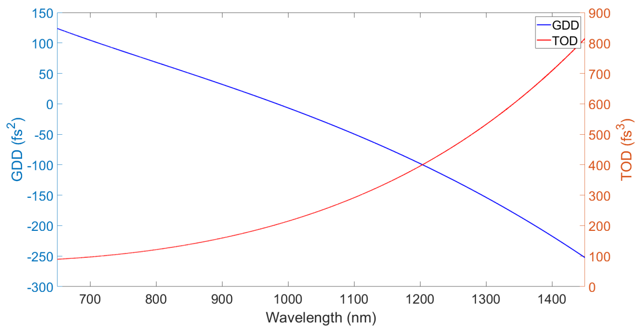

Figure 4.11: GDD and TOD as a function of wavelength for KDP obtained from the ordinary refractive index (n_o) expression from the Sellmeier equations. A thickness of 2.5 mm of KDP was considered, which will later be implemented experimentally.

Following discussions on this matter, we decided to test propagating the pulses through a certain thickness of Potassium Dihydrogen Phosphate (KDP) and through more Fused Silica (FS). KDP is a commonly used nonlinear crystal for pulse compression due to its TOD characteristics. After several tests, promising results were observed through the propagation of each pulse in 5 mm of KDP and 5 mm of FS virtually in the dispersion-scan software. Figure 4.11 shows the GDD and TOD tendencies of KDP for a wavelength range from 700 nm to 1400 nm, which is approximately the same as the spectral broadening interval. At a wavelength of 1.03 μm, the GDD value tends towards 0, therefore showing a lack of application for the second order dispersion. Regarding the TOD for this wavelength at value of + 235 fs^3 renders which shows it will increase the negative TOD of the incoming pulse. For larger wavelengths it varies largely but smoothly while maintaining an overall positive GDD. This will allow for a controlled compensation of the third order without introducing distortions in the second order. The reason KDP was chosen was due to its larger values for TOD compensation compared to FS, allowing a more efficient dispersion management for a short propagation length.

The results of these simulations are shown in Figures 4.12 and 4.13.

Comparing both heat maps in Figures 4.9 and 4.12, it is clear to see the vanishing of the side pulses as well as a converging of the shape of the pulse. The newly compressed pulses appear more condensed towards a single peak of slightly stronger intensity.

Their shapes are better shown in Figure 4.13 where there is also a clear decrease in the pulse duration of each pulse. Therefore we can safely say that propagation through both these materials will only help the compression of the pulse.

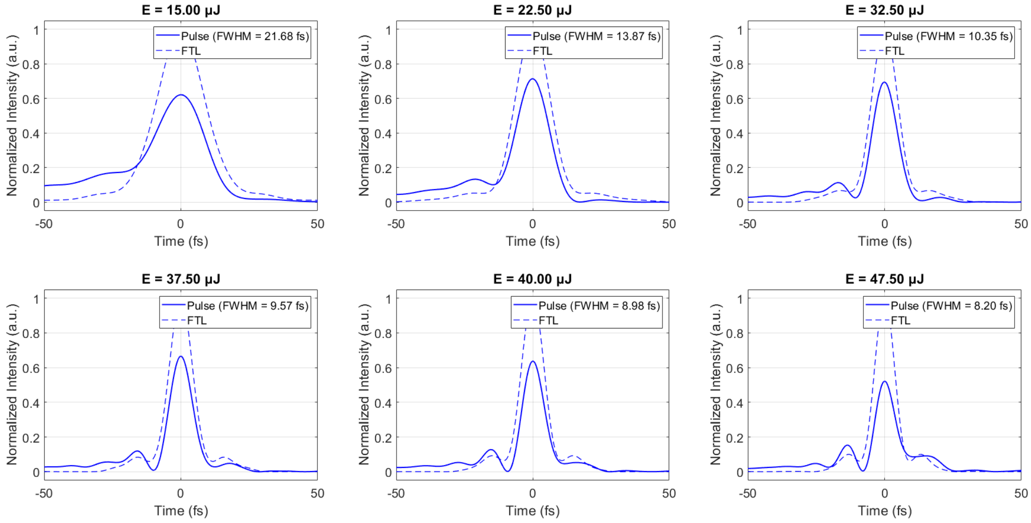

Figure 4.13: Retrieved Output Pulse Temporal Profiles of MPC 2 for certain incoming pulse energies considering virtual propagation through 5 mm of KDP and 5 mm of FS. The pulse retrievals were obtained for 0 mm insertion of dispersion.

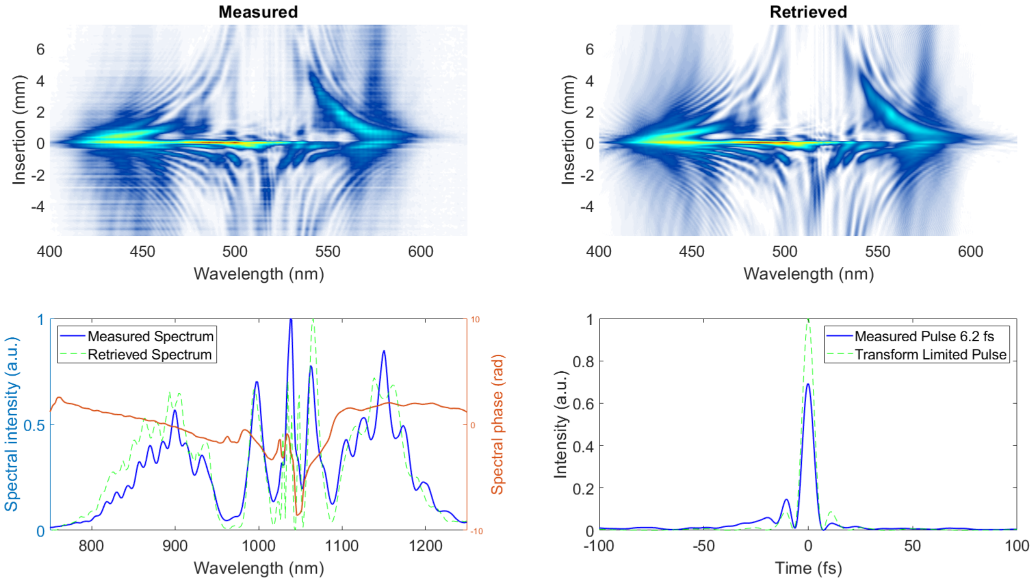

Figure 4.14: D-Scan Retrieval for E_{in} = 68.75 μJ, FS Plates Separation 17 cm, Propagation through 2.5 mm KDP and 1.5 mm FS. The spectrum acquired on the lower left graph is for 0 mm of dispersion insertion.

The final step carried out was to experimentally implement the propagation through KDP and FS. Firstly the number of bounces on the chirped mirrors of the compression stage was altered to 2 bounces on one mirror and 1 bounce on the other. This was carried out to compensate the uneven number of bounces of the beam on the cavity mirrors. Although the roundtrips are being achieved, due to the presence of the in-/out-coupling mirror, one cavity mirror has a bounce less than the other. Therefore this is now compensated by an uneven number of bounces on the compression stage. Additionally, this decrease in separation of the CM also allows for the FS added to stabilize the GDD of the system.

The FS was added in the form of 2 wedges in order to manage the amount of insertion and the KDP was added in the form of a 2.5 mm thick plate. To observe the outcomes better, the energy was scaled up higher and 1.5 mm of FS was inserted. Results are shown in Figure 4.14 where a compressed pulse with duration of 6.2 fs is retrieved without further changes being made. The measured FTL duration was 5.67 fs.

The incoming energy from MPC 1 to MPC 2 was approximately 69 μJ, while the energy of the pulse out-coupled from the cell (before the compression stage) was 40 μJ, rendering an efficiency of the cell of 60%. Then, finally after the compression stage, the energy was measured to be 38 μJ. Taking this value, it is possible to obtain the peak power of the 6.2 fs long pulse: 5.76 GW.

This result is quite remarkable, proving that the few-cycle regime can be achieved. As the laser central wavelength is 1030 nm, the duration for single-cycle is 3.43 fs. Therefore the obtained compressed pulse lasts below 2 optical cycles.

It is also possible to write out the B-integral as was done with the previous spectra measurements. The spectral broadening of the 6.2 fs pulse (Figure 4.14, bottom left) is 308.85 nm at FWHM. Using Equation 2.30 with this spectral broadening as the output at $\Delta\nu_{in} = 47.37$ nm, the spectral broadening of MPC 1, the value of the B-integral is 7.34 rad, which provides an accumulated nonlinear phase shift per pass of 0.52 rad. This value is also below the bound of $\pi/5$ [21].

4.3.3 Laser Beam Profile

Observing the beam profile is an important parameter for its characterization. The beam shape provides a lot of information on the efficiency of the setup; for instance, there could be some clipping on some optical elements or some aberrations could also be introduced.

Before the additional FS wedges and the KDP plate were added, some images were taken of the cross section of the beam at different energies when the FS plates were located 17 cm apart from each other, shown in Figures 4.15. Overall the tendency of the beams is quite stable, maintaining an elliptical shape with constant sizes. As a side note, there is a slight increase in the ellipse along the vertical direction for higher incoming energies. The beam seems to elongate more along the y-axis (Figure 4.15d). This is caused by the Kerr Effect induced by the nonlinear plates. Since the pulse energy is higher the intensity going into the fused silica will cause more self-focusing to take place.

M^2 Measurements

In order to further characterize the 6.2 fs pulse obtained we proceeded to observe the spatial characteristics of the beam. To do so, it was propagated and then focused with a lens. Several images were taken for different positions along the focal point and the beam diameters along the x- and y-axes were extracted. All parameters were fitted to hyperbolas and the results are shown in Figure 4.16.

M_x^2	3.423
Beam waist w_0^x	151.98 μm
Waist Position z_0^x	141.61 mm
Rayleigh Range z_R^x	20.58 mm
M_y^2	2.916
Beam waist w_0^y	137.28 μm
Waist Position z_0^y	138.70 mm
Rayleigh Range z_R^y	19.71 mm

Table 4.4: MPC 2 M^2 Measurement results

The values retrieved are shown in Table 4.4. These values can be compared to the M^2 values of the laser output for the same settings. Considering an energy of 1 mJ with repetition rate 8 kHz and 2% noise removal, the measured laser M^2 values are: M$_x^2$ = 1.00 and M$_y^2$ = 1.17.

From these measurements it was also possible to extract the focus image of the beam, which is shown in Figure 4.17.

The values measured for the M^2 measurements are quite far from 1 and even from the beam quality of the laser output. These values are then considered inconclusive as they cannot provide any information on the focusability or quality of the laser beam coming out of MPC 2. As a reference, the optimal values for the beam quality factor are between 1 and 1.5. Values over 2 no longer make sense and do not give information on the focusability of the beam.

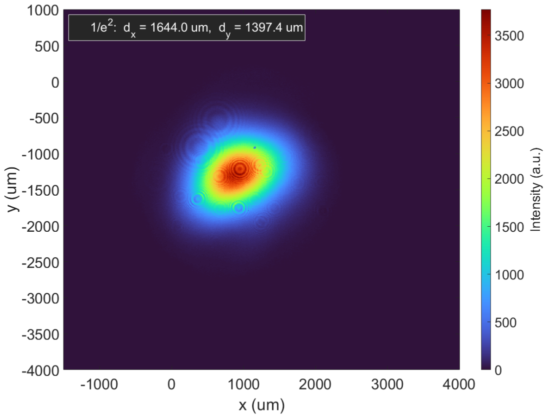

(a) E$_{in}$ = 12.5 μJ

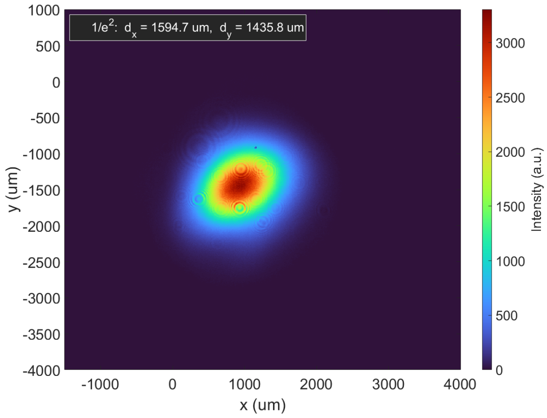

(b) E$_{in}$ = 20 μJ

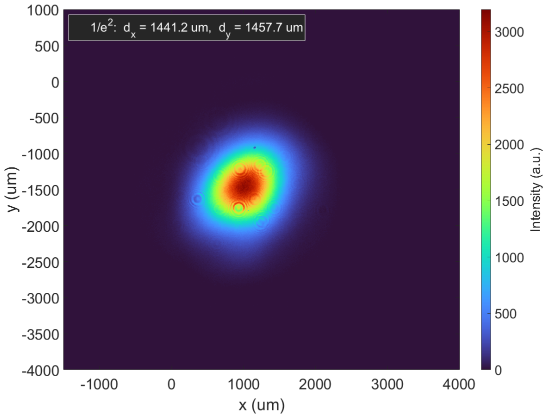

(c) E$_{in}$ = 30 μJ

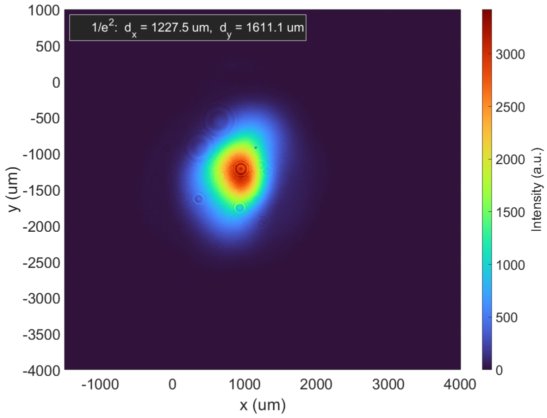

(d) E$_{in}$ = 47.5 μJ

Figure 4.15: Collimated Beam Profile of MPC 2 FS for Plate Separation 17 cm

However, the reasoning for the poor results obtained from this beam quality study is due to the incompatibility between the camera used to take the beam profiles and the spectrum that is being measured. As shown in Figure 4.14, the short pulse that is being measured has an extremely large spectral broadening, ranging from 800 nm to 1300 nm approximately. This renders an issue with the camera that is being used, which consists on a silicon detector. These are only compatible with spectra up to 1100 nm and wavelengths above are not being captured. Therefore, due to this limiting factor, it is impossible to conclude regarding the beam quality and the beam profile of the output beam from MPC 2.

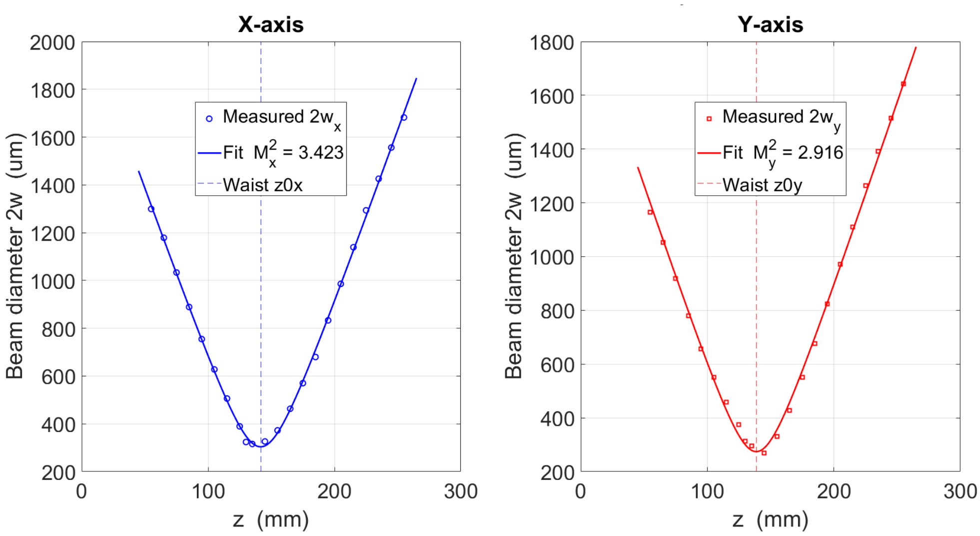

Figure 4.16: M^2 Measurement of Outcoming Pulse

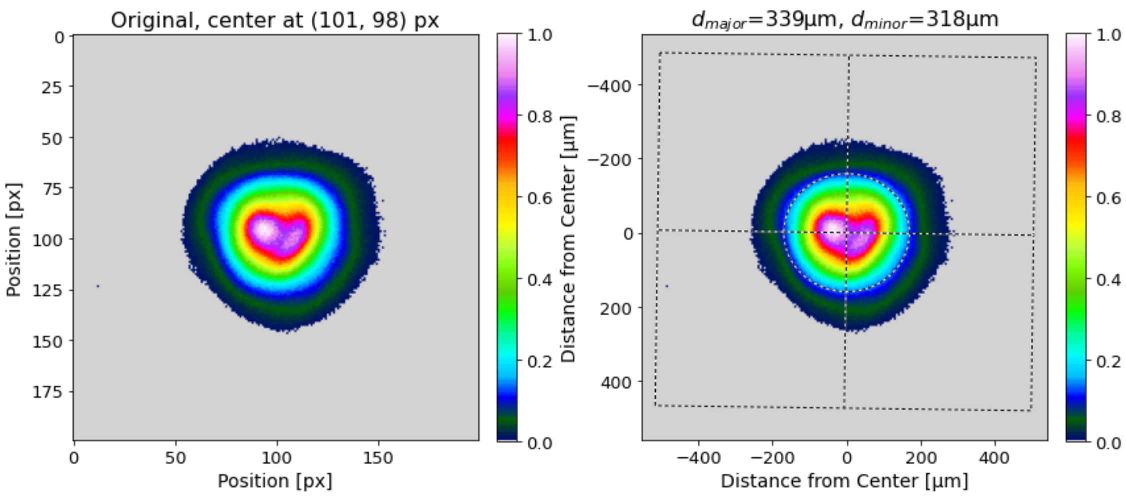

Figure 4.17: Measured Focus from MPC 2 Output using a Focusing Lens

Chapter 5

Conclusions and Outlook

In this work, we have implemented a second stage multi-pass cell to a cascaded architecture in order to achieve further pulse compression. From an existing first stage (MPC 1), an already compressed pulse had been achieved, rendering time durations of 50 fs and through MPC 2, pulses in the few-cycle regime were achieved.

5.1 Conclusions

Multi-pass cells are a common pulse post-compression technique that exploit the optical Kerr effect. A laser pulse with time-varying intensity will induce a time-dependent refractive index leading to self-phase modulation (SPM) to take place. This is visible through spectral broadening of the incoming laser pulse spectrum. SPM comes from media placed inside the cavity that will induce the nonlinearities. The nonlinear medium also induces dispersion to the pulse. The cascaded setup was used as it has proven to show good efficiency.

The objective to achieve an outcoming pulse with 2-3 optical cycles altered the design of MPC 2 compared to MPC 1. The first stage was made up of non-dispersion-compensating focusing mirrors to make up the cavity and this was feasible since the rendered pulses were not few-cycle, thus the spectrum was not as broad. But since this aspect changed for the second stage, dielectric mirrors were required supporting octave-spanning bandwidths to act as dispersion-matched mirror pairs. These novel mirrors compensated for the second order dispersion gained through the propagation in the nonlinear plates within each roundtrip, but not for the phase shift of the pulse from the SPM. Both cells were thought up as Herriott type, where the re-entrant condition would provide an out-coupled beam with the same characteristics as the in-coupled beam, to ensure beam stability. Additionally, from the preknown radii of curvature for the cell mirrors and how many roundtrips were desired, the cell length was extracted. The nonlinear media for both were 2 times 1 mm fused silica plates (bulk). In MPC 2 they were placed at Brewster angle for transmission optimization increasing the propagation distance to 1.215 mm for each.

Focusing now on the results obtained from MPC 2, the spectra show the effects of the spectral broadening and its dependence on the nonlinear plate separation as well as incoming energy. The results showed more broadening for larger input energies, aligning with the theoretical expectation from the intensity dependence. Regarding the plate separation, several steps were studied for which it was observed that the closer the plates are, larger spectral broadening renders. This is due to the fact of the self-focusing effect acting much more strongly. The drawback is that the supported energy is limited for closer plates because this setting increases the intensity much more. This will only push the system closer to the limits of self-focusing, which are beam degradation or damaging the bulk plates. Another possible limitation that can be reached is spectral saturation.

For the final step of pulse compression the largest plate separation was chosen in order to work with a larger input energy range. The closer separation would have also provided large spectral broadening but the outcoming beam and phase were quite poor. The characterization of all the pulses was carried out through a dispersion-scan which measures the laser pulse right after the compression stage. Additionally, the software also allows to virtually propagate the measured pulse to add or remove different materials in order to fine tune the dispersion. This is done by changing the second and third order phase terms in order to optimize the compression of the pulse and its quality. Once the compression stage had been set up with one bounce on each chirped mirror, an initial measurement was taken. The outcome was that further GDD compensation was required, thus prompting to increase the bounces to 2 on each mirror. From this new setup a larger energy study was performed. The results showed compressed pulses but tampered by the presence of a pedestal, especially for the larger input energies. Additionally, the phases of the pulses were quite irregular, showing a strong TOD presence for all. This may have appeared from the bulk plates as well as the chirped mirrors. However, unlike the GDD, TOD does not cancel out in the same manner. Therefore it was necessary to include some elements to control this higher dispersion. KDP was considered for its known GDD and TOD characteristics to increase the TOD for the 1 μm central wavelength. Additionally, from the setup of the second stage, as the in-/out-coupling mirror is placed closer to the cavity mirrors, there was one bounce less on one of the cell mirrors. This was then balanced by having an uneven number of bounces on the compression stage mirrors. This new setup rendered quite positive results of a 6.2 fs laser pulse, below a 2-cycle pulse. In terms of temporal features, the pulse compression was quite efficient as it came quite close to the FTL which had a time duration of 5.67 fs. An attempted study of the spatial characteristics was made, where both the beam profile and quality were observed. For both, a camera is required, however now there is the limiting factor of an extremely large spectral bandwidth. The camera used included a silicon detector which only measured up to a wavelength of 1100 nm, which is insufficient for our few-cycle pulse. Therefore, this meant a large section of the pulse being left out of the study and so the results being inconclusive. Nonetheless, this study can be fully carried out with the correct camera with a wavelength range fully in the near-infrared (from 700 nm to 1400 nm, approximately).

5.2 Outlook

The goal of this project was to build a cascaded system of multi-pass cells for pulse compression to finally achieve the few-cycle regime. The desired results were achieved with a pulse duration of 6.2 fs. However, some possible steps are also left to improve to optimize the technique and setup.

The first continuation of this work would be to push the limits of the setup slightly to achieve shorter pulse durations. This could be achieved by increasing even more the input energy into the cell to observe the behavior, which is currently limited by the output pulse energy of the first stage. Should the energy reach close to the limitations, a possible fix is to increase the bulk plate separation. The combination of both steps would, according to theory, provide more spectral broadening. Although, as we were surprised by the sudden presence of higher order dispersion, it could also be the case that their presence is stronger requiring further compensation.

A second continuation for the project would be to carry out the spatial characterization of the laser beam with better suited electronics. This would be interesting as it will provide a wide range of information from the shape and size of the collimated beam to its focusability. The latter is quite an important feature considering the purpose of this newly generated few-cycle pulse because high intensity and tightly focused laser beams are required for HHG. The focus currently measured provides an initial idea of the potential shape this beam could focus down to. Similarly, the images of the collimated beam also provided a pre-knowledge to the overall shape of the beam. However, due to the missing information, these conclusions are only indicative of the beam quality.

Another feature to improve could be the efficiency of MPC 2, as it is currently at 60% transmission. This is already an appropriate value considering the presence of the chirped cavity mirrors as well as many un-coated optical elements. Nevertheless, there is a large loss from the input energy to the output of the cell. In fact, the incorporation of the KDP plate and FS wedges decreases the energy value some more.

However, overall during the building of the cell, it was observed the robustness of the setup proving long-term stability in terms of alignment, as it was quite fast and straightforward to align the cell to find the optimal efficiency. Robustness was already a known advantage of bulk multi-pass cells however observing it experimentally confirmed the design choices. The results obtained from this cascade of MPCs have shown promising, rendering results close to previous experiments [16]. One particularity from the cell built in this project is the compression stage, which is not the classical chirped mirror pair only, but also accounts with a KDP plate and FS wedges for further fine-tuning. A planned future change to the setup is to include thickness-varying KDP element, such as a wedge, in order to be able to fine tune its insertion. This will also contribute to the compression of pulses at different energies.

A final idea of further study with this setup would be to look into the results obtained when the beam is no longer a Gaussian (Laguerre-Gaussian 00 LG_{00}) but rather with a higher-mode beam or a vortex LG_{lp}, which has already been studied for HHG optimization [41]. This can be achieved through a Spatial Light Modulator (SLM), which is a device that controls the intensity, phase and polarization of light in space. It would be quite interesting to observe the temporal outcome of the pulse as well as the spectral broadening for such type of beam, in comparison to the usual Gaussian.

To sum up, the overall goal of the thesis was achieved as the end result is below a 2-cycle pulse with duration 6.2 fs. This was achieved through a cascaded system of 2 bulk multi-pass cells where the second consisted on a dispersion-managed cell. Some important key takeaways learned from this project include the different steps of the building (parts of the setup) followed by the iterative compression design. Throughout the process different issues rose such as TOD presence, which was observed to not cancel out in such a straight-forward manner as the GDD. Additionally, small asymmetries in the setup, such as the uneven number of bounces on the cell mirrors, have larger effects on the setup proving the sensitivity of such post-compression systems.

The few-cycle pulses produced in this cascaded architecture of MPCs show a practical, robust and energy-scalable option of pulse control for high-harmonic generation experiments, where high peak intensities and broad bandwidths are fundamental.

Bibliography

[1] Theodor Maiman. Stimulated optical radiation in ruby. *Nature*, 187:493–494, 1960. URL https://doi.org/10.1038/187493a0.

[2] H. Abu-Shawareb, R. Acree, and Adams. Lawson criterion for ignition exceeded in an inertial fusion experiment. *Phys. Rev. Lett.*, 129:075001, Aug 2022. doi: 10.1103/PhysRevLett.129.075001. URL https://link.aps.org/doi/10.1103/PhysRevLett.129.075001.

[3] C M Heyl, J Güdde, A L'Huillier, and U Höfer. High-order harmonic generation with j laser pulses at high repetition rates. *Journal of Physics B: Atomic, Molecular and Optical Physics*, 45(7):074020, mar 2012. doi: 10.1088/0953-4075/45/7/074020. URL https://doi.org/10.1088/0953-4075/45/7/074020.

[4] Ferenc Krausz and Misha Ivanov. Attosecond physics. *Rev. Mod. Phys.*, 81:163–234, Feb 2009. doi: 10.1103/RevModPhys.81.163. URL https://link.aps.org/doi/10.1103/RevModPhys.81.163.

[5] E. Esarey, C. B. Schroeder, and W. P. Leemans. Physics of laser-driven plasma-based electron accelerators. *Rev. Mod. Phys.*, 81:1229–1285, Aug 2009. doi: 10.1103/RevModPhys.81.1229. URL https://link.aps.org/doi/10.1103/RevModPhys.81.1229.

[6] Donna Strickland and Gerard Mourou. Compression of amplified chirped optical pulses. *Optics Communications*, 56(3):219–221, 1985. ISSN 0030-4018. doi: https://doi.org/10.1016/0030-4018(85)90120-8. URL https://www.sciencedirect.com/science/article/pii/0030401885901208.

[7] Angana Mondal, Benedikt Waser, Tadas Balciunas, Ofer Neufeld, Zhong Yin, Nicolas Tancogne-Dejean, Angel Rubio, and Hans Jakob Wörner. High-harmonic generation in liquids with few-cycle pulses: effect of laser-pulse duration on the cut-off energy. *Optics Express*, 31(21):34348, September 2023. ISSN 1094-4087. doi: 10.1364/oe.496686. URL http://dx.doi.org/10.1364/OE.496686.

[8] Tamas Nagy, Peter Simon, and Laszlo Veisz. High-energy few-cycle pulses: post-compression techniques. *Advances in Physics: X*, 6(1):1845795, 2021. doi: 10.1080/23746149.2020.1845795. URL https://doi.org/10.1080/23746149.2020.1845795.

[9] M. Nisoli, S. De Silvestri, and O. Svelto. Generation of high-energy 10-fs pulses by a new pulse compression technique. In *Conference on Lasers and Electro-Optics*, page CTuR5. Optica Publishing Group, 1996. URL https://opg.optica.org/abstract.cfm?URI=CLEO-1996-CTuR5.

[10] Binhammer T. Steingrube D.S. et al. Schulz, E. Intense few-cycle laser pulses from self-compression in a self-guiding filament. *Appl. Phys. B*, 95:269 – 272, 2009. URL https://doi.org/10.1007/s00340-009-3456-5.

[11] Ming-Shian Tsai, An-Yuan Liang, Chia-Lun Tsai, Po-Wei Lai, Ming-Wei Lin, and Ming-Chang Chen. Nonlinear compression toward high-energy single-cycle pulses by cascaded focus and compression. *Science Advances*, 8(31):eabo1945, 2022. doi: 10.1126/sciadv.abo1945. URL https://www.science.org/doi/abs/10.1126/sciadv.abo1945.

[12] Anne-Lise Viotti, Marcus Seidel, Esmerando Escoto, Supriya Rajhans, Wim P. Leemans, Ingmar Hartl, and Christoph M. Heyl. Multi-pass cells for post-compression of ultrashort laser pulses. *Optica*, 9(2):197–216, Feb 2022. doi: 10.1364/OPTICA.449225. URL https://opg.optica.org/optica/abstract.cfm?URI=optica-9-2-197.

[13] Martin Kaumanns, Dmitrii Kormin, Thomas Nubbemeyer, Vladimir Pervak, and Stefan Karsch. Spectral broadening of 112mj, 1.3ps pulses at 5khz in a lg10 multipass cell with compressibility to 37fs. *Opt. Lett.*, 46(5):929–932, Mar 2021. doi: 10.1364/OL.416734. URL https://opg.optica.org/ol/abstract.cfm?URI=ol-46-5-929.

[14] K. C. Kulander, K. J. Schafer, and J. L. Krause. Dynamics of short-pulse excitation, ionization and harmonic conversion. In M. G. Blain, G. D. Tipton, W. M. Holber, P. L. Westerfield, and K. L. Maxwell, editors, *Presented at the NATO Workshop*, pages 8–14, January 1993.

[15] S. Westerberg, M. Redon, A.-K. Raab, G. Beaufort, M. Arias Velasco, C. Guo, I. Sytcevich, R. Weissenbilder, D. O'Dwyer, P. Smorenburg, C. L. Arnold, A. L'Huillier, and A.-L. Viotti. Influence of the laser pulse duration in high-order harmonic generation. *APL Photonics*, 10 (9):096103, 09 2025. ISSN 2378-0967. doi: 10.1063/5.0272968. URL https://doi.org/10.1063/5.0272968.

[16] Michael Müller, Joachim Buldt, Henning Stark, Christian Grebing, and Jens Limpert. Multipass cell for high-power few-cycle compression. *Opt. Lett.*, 46(11):2678–2681, Jun 2021. doi: 10.1364/OL.425872. URL https://opg.optica.org/ol/abstract.cfm?URI=ol-46-11-2678.

[17] Anne-Lise Viotti, Chen Li, Gunnar Arisholm, Lutz Winkelmann, Ingmar Hartl, Christoph M. Heyl, and Marcus Seidel. Few-cycle pulse generation by double-stage hybrid multi-pass multi-plate nonlinear pulse compression. *Opt. Lett.*, 48(4):984–987, Feb 2023. doi: 10.1364/OL.478790. URL https://opg.optica.org/ol/abstract.cfm?URI=ol-48-4-984.

[18] Hermann A Haus. Theory of mode locking with a fast saturable absorber. *Journal of Applied Physics*, 46(7):3049–3058, 1975.

[19] Bahaa E A Saleh and Malvin Carl Teich. *Fundamentals of photonics*. Wiley series in pure and applied optics. Wiley, New York, NY, 2007. URL https://cds.cern.ch/record/1084451.

[20] E. Esarey, C. B. Schroeder, and W. P. Leemans. Physics of laser-driven plasma-based electron accelerators. *Rev. Mod. Phys.*, 81:1229–1285, Aug 2009. doi: 10.1103/RevModPhys.81.1229. URL https://link.aps.org/doi/10.1103/RevModPhys.81.1229.

[21] Victor Hariton, Kilian Fritsch, Kevin Schwarz, Nazar Kovalenko, Gonçalo Figueira, Gunnar Arisholm, and Oleg Pronin. Spectral broadening in convex-concave multipass cells. *Opt. Express*, 31(12):19554–19568, Jun 2023. doi: 10.1364/OE.486797. URL https://opg.optica.org/oe/abstract.cfm?URI=oe-31-12-19554.

[22] Marcus Seidel, Prannay Balla, Chen Li, Gunnar Arisholm, Lutz Winkelmann, Ingmar Hartl, and Christoph M. Heyl. Factor 30 pulse compression by hybrid multipass multiplate spectral broadening. *Ultrafast Science*, 2022, 2022. doi: 10.34133/2022/9754919. URL https://spj.science.org/doi/abs/10.34133/2022/9754919.

[23] Tamas Nagy, Peter Simon, and Laszlo Veisz. High-energy few-cycle pulses: post-compression techniques. *Advances in Physics: X*, 6(1):1845795, 2021. doi: 10.1080/23746149.2020.1845795. URL https://doi.org/10.1080/23746149.2020.1845795.

[24] A. Dubietis, G. Jonušauskas, and A. Piskarskas. Powerful femtosecond pulse generation by chirped and stretched pulse parametric amplification in bbo crystal. *Optics Communications*, 88(4):437–440, 1992. ISSN 0030-4018. doi: https://doi.org/10.1016/0030-4018(92)90070-8. URL https://www.sciencedirect.com/science/article/pii/0030401892900708.

[25] J. C. Knight, T. A. Birks, P. St. J. Russell, and D. M. Atkin. All-silica single-mode optical fiber with photonic crystal cladding. *Opt. Lett.*, 21(19):1547–1549, Oct 1996. doi: 10.1364/OL.21.001547. URL https://opg.optica.org/ol/abstract.cfm?URI=ol-21-19-1547.

[26] Chih-Hsuan Lu, Yu-Jung Tsou, Hong-Yu Chen, Bo-Han Chen, Yu-Chen Cheng, Shang-Da Yang, Ming-Chang Chen, Chia-Chen Hsu, and A. H. Kung. Generation of intense supercontinuum in condensed media. *Optica*, 1(6):400–406, Dec 2014. doi: 10.1364/OPTICA.1.000400. URL https://opg.optica.org/optica/abstract.cfm?URI=optica-1-6-400.

[27] Chih-Hsuan Lu, Wei-Hsin Wu, Shiang-He Kuo, Jhan-Yu Guo, Ming-Chang Chen, Shang-Da Yang, and A. H. Kung. Greater than 50 times compression of 1030 nm yb:kgw laser pulses to single-cycle duration. *Opt. Express*, 27(11):15638–15648, May 2019. doi: 10.1364/OE.27.015638. URL https://opg.optica.org/oe/abstract.cfm?URI=oe-27-11-15638.

[28] Robert Szipöcs, Kárpát Ferencz, Christian Spielmann, and Ferenc Krausz. Chirped multilayer coatings for broadband dispersion control in femtosecond lasers. *Opt. Lett.*, 19(3):201–203, Feb 1994. doi: 10.1364/OL.19.000201. URL https://opg.optica.org/ol/abstract.cfm?URI=ol-19-3-201.

[29] E. Treacy. Optical pulse compression with diffraction gratings. *IEEE Journal of Quantum Electronics*, 5(9):454–458, 1969. doi: 10.1109/JQE.1969.1076303.

[30] S. Gröbmeyer, K. Fritsch, B. Schneider, et al. Self-compression at 1 µm wavelength in all-bulk multi-pass geometry. *Applied Physics B*, 126:159, 2020. doi: 10.1007/s00340-020-07506-4.

[31] Laura Silletti, Ammar bin Wahid, Esmerando Escoto, Prannay Balla, Supriya Rajhans, Katinka Horn, Lutz Winkelmann, Vincent Wanie, Andrea Trabattoni, Christoph M. Heyl, and Francesca Calegari. Dispersion-engineered multi-pass cell for single-stage post-compression of an ytterbium laser. *Opt. Lett.*, 48(7):1842–1845, Apr 2023. doi: 10.1364/OL.476846. URL https://opg.optica.org/ol/abstract.cfm?URI=ol-48-7-1842.

[32] Kazunori Naganuma, Kazuo Mogi, and Hajime Yamada. General method for ultrashort light pulse chirp measurement. *IEEE Journal of Quantum Electronics*, 25:1225–1233, 1989. URL https://api.semanticscholar.org/CorpusID:122587862.

[33] Rick Trebino. *Frequency-Resolved Optical Gating: The Measurement of Ultrashort Laser Pulses*, pages 117–139. Kluwer Academic Press, 01 2000. ISBN 978-1-4613-5432-1.

[34] M. Miranda, H. Crespo, et al. Method and apparatus for characterization and compression of ultrashort laser pulses, 2014. Basis of the d-scan technique.

[35] Miguel Miranda, Chen Guo, Paulo Guerreiro, Cord Arnold, Vítor Amorim, and Rosa Romero. dispersion-scan ultrashort pulse characterization implemented with a 4-f pulse stretcher/compressor. 1 2026. doi: 10.1364/opticaopen.31100479.v1. URL https://preprints.opticaopen.org/articles/preprint/dispersion-scan_ultrashort_pulse_characterization_implemented_with_a_4-f_pulse_stretcher_compressor/31100479.

[36] Jan Schulte, Thomas Sartorius, Johannes Weitenberg, Andreas Vernaleken, and Peter Russbueldt. Nonlinear pulse compression in a multi-pass cell. *Optics letters*, 41(19):4511–4514, 2016.

[37] Donald R. Herriott and H. J. Schulte. Folded optical delay lines. *Applied Optics*, 4:883–889, 1965. URL https://api.semanticscholar.org/CorpusID:73575060.

[38] Esmerando Escoto, Anne-Lise Viotti, Skirmantas Alisauskas, Henrik Tünnermann, Ingmar Hartl, and Christoph M. Heyl. Temporal quality of post-compressed pulses at large compression factors. *J. Opt. Soc. Am. B*, 39(7):1694–1702, Jul 2022. doi: 10.1364/JOSAB.453901. URL https://opg.optica.org/josab/abstract.cfm?URI=josab-39-7-1694.

[39] G. Arisholm and H. Fonnum. Simulation system for optical science (sisyfos) - tutorial, version 2. *Norwegian Defence Research Establishment (FFI)*, 2021.

[40] Ann-Kathrin Raab, Marcus Seidel, Chen Guo, Ivan Sytcevich, Gunnar Arisholm, Anne L'Huillier, Cord L. Arnold, and Anne-Lise Viotti. Multi-gigawatt peak power post-compression in a bulk multi-pass cell at a high repetition rate. *Opt. Lett.*, 47(19):5084–5087, Oct 2022. doi: 10.1364/OL.463960. URL https://opg.optica.org/ol/abstract.cfm?URI=ol-47-19-5084.

[41] Alba de las Heras, Alok Kumar Pandey, Julio San Román, Javier Serrano, Elsa Baynard, Guillaume Dovillaire, Moana Pittman, Charles G. Durfee, Luis Plaja, Sophie Kazamias, Olivier Guilbaud, and Carlos Hernández-García. Extreme-ultraviolet vector-vortex beams from high harmonic generation. *Optica*, 9(1):71–79, Jan 2022. doi: 10.1364/OPTICA.442304. URL https://opg.optica.org/optica/abstract.cfm?URI=optica-9-1-71.